FINE STRUCTURE IN THERMAL NEUTRON (n,α) REACTIONS

FINE STRUCTURE IN THERMAL NEUTRON (n,α) REACTIONS

by

NEIL STANLEY OAKEY, B.Sc.,M.Sc.

A Thesis

Submitted to the Faculty of Graduate Studies

in Partial Fulfilment of the Requirements

for the Degree

Doctor of Philosophy

McMaster University

September 1967

DOCTOR OF PHILOSOPHY (1967)
(Physics)

McMASTER UNIVERSITY
Hamilton, Ontario

TITLE: Fine Structure in Thermal Neutron (n,α) Reactions

AUTHOR: Neil Stanley Oakey, B.Sc. (McGill University)
M.Sc. (University of Saskatchewan)

SUPERVISOR: Dr. R. D. Macfarlane

NUMBER OF PAGES: viii, 96

SCOPE AND CONTENTS:

Fine structure in thermal neutron (n,α) reactions has been studied for ^{149}Sm, ^{147}Sm, and ^{143}Nd by means of an instrument called an electrostatic particle guide. This device, which was designed to eliminate the problems of background and low energy tailing in (n,α) spectroscopy, is described in detail. Alpha decay has been observed from thermal neutron capture states to levels in the daughter nucleus to greater than 2 MeV excitation. Cross sections and alpha energies are presented for each transition and as well, the alpha decay schemes for ^{146}Nd, ^{144}Nd, ^{140}Ce. Experimental reduced widths have been calculated and are discussed in terms of Mang's theory of alpha decay. Evidence is presented for the (n, Yα) process in the ^{143}Nd (n,α) ^{140}Ce reaction.

ACKNOWLEDGEMENTS

I wish to thank the members of my Supervisory Committee, Dr. R. D. Macfarlane, Dr. R. G. Summers-Gill and Dr. J. Cameron whose interest in my research project and whose suggestions have been most useful. In particular, I am indebted to my Research Director, Dr. R. D. Macfarlane, who suggested the problem and followed its progress with keen interest and suggestions when most needed.

Thanks are due also to the members of the Nuclear Research Shop, and in particular Mr. T. Bryden and Mr. H. Howell, who have helped with the design and fabrication of various instruments. Without the reactor these experiments would not have been possible and it is therefore with thanks that the cooperation and help of the staff of the McMaster reactor is acknowledged.

I wish to thank Mr. M. C. Gupta who helped with computer programming and Mr. K. Beg who supplied useful prepublication data on alpha energies and cross sections.

My wife, Nora, deserves the greatest thanks for her help and moral support during my years in graduate school.

Financial support by the Province of Ontario is gratefully acknowledged.

TABLE OF CONTENTS

TABLE OF CONTENTS

LIST OF TABLES

LIST OF ILLUSTRATIONS

LIST OF ILLUSTRATIONS

CHAPTER I

INTRODUCTION

Since the discovery that certain naturally occurring elements emit alpha particles, the study of alpha-radioactivity has yielded much invaluable information to the nuclear spectroscopist.

Alpha decay, in contrast to beta and gamma radiation, is only mildly inhibited by changes in angular momentum. One expects, therefore, to populate most low-lying levels of the daughter nucleus. As a spectroscopic tool, alpha-radiation suffers from two limitations. It is restricted to certain regions of the periodic table and the transition probability is very sensitively dependent on alpha energy. Consequently, the alpha intensity decreases rapidly as the excitation of the daughter nucleus increases.

In recent years, alpha decay following thermal neutron capture has been observed in weak competition with gamma decay[1,2]. Aside from the light elements where the Coulomb barrier is small, two other regions are very favorable: above the 50 proton closed shell and in the rare earth region above the 82 neutron closed shell. Studies in this latter region are the subject of this thesis.

A basic difference between natural alpha decay and the (n, α) reaction is that in the latter case alpha decay is from a complicated state at high excitation, whereas in the former case the transition is usually from the ground state. In the discussion which follows, the main

features of alpha decay are considered with particular reference to (n, α) reactions.

One of the early triumphs of quantum mechanics was the explanation by Gamow[3] and independently by Condon and Gurney [4] of the sensitive dependence of alpha decay rate on the alpha energy. Their simple one body model considered the alpha particle as moving in a potential-well created by the remaining nucleons and the Coulomb barrier. At each collision of the alpha particle with the potential barrier there is a probability of escaping, the penetrability, P. Thus the decay constant, λ , is given by the product of the collision frequency with the wall and the penetrability:

$$\lambda = f P = \frac{v}{2R} P \quad . \qquad 1.1$$

In this expression, v is the alpha velocity and R is the radius of the potential well.

This model is plausible only if the alpha particle can move as an entity in the nuclear volume. If one specifies a nuclear radius, R , surface thickness, s , and alpha mean free path, ℓ_a , then the simple model is valid only if $\ell_a > R$. If $\ell_a \approx s$ then the alpha particle cannot exist as a well-defined entity in nuclear matter and the notion of an alpha-nuclear potential may have meaning only in the surface region. From the analysis of alpha-scattering data it is found that $\ell_a \approx 1$ fm $\approx s$ [5,6]. Thus, while the decay constant can still be considered as a product of frequency and penetrability terms, these terms are evidently more complicated than in the one body model.

In Winslow's "surface-well model" [7] the approach is modified by considering that the alpha particle is formed at the surface. He proposed a surface-well potential with a repulsive potential in the interior. In this model the frequency factor is replaced by the probability of forming an alpha particle in the nucleus, the formation factor.

The first many body approach to alpha decay was formulated by Thomas [8] but he did not apply it to a nuclear model to calculate decay rates. Mang [9,10] applied the many body approach to the shell model with great success in explaining alpha decay of even-even spherical nuclei. It is his approach which will be outlined here.

Alpha decay and (n, α) reactions must obey certain conservation laws. Conservation of energy requires that the kinetic energy of the final system at large separation, Q_f , be given by

$$Q_f = (M_{A+4} - M_A - M_{He^4}) c^2 \qquad 1.2$$

where M_{A+4} , M_A , and M_{He^4} are the nuclear masses of the parent, daughter and alpha particle respectively and c is the velocity of light. For thermal neutron (n, α) reactions this becomes

$$Q_f = (M_{A+3} + M_n - M_A - M_{He^4}) c^2 \qquad 1.3$$

where M_n is the mass of the neutron. Conservation of linear momentum requires that the total kinetic energy be divided between the two products in inverse proportion to their masses. The value, Q_f , which is desired for calculations is different from the value, Q , measured in the laboratory since one is dealing with nuclei which have an electron cloud. Q_f may be obtained by adding to Q the screening correction, ΔE_{sc} , which

represents the energy the alpha particle loses in doing work against the attractive electron cloud as it leaves the nucleus. This correction is given by

$$\Delta E_{sc} = 65.3\ Z^{7/5} - 80\ Z^{2/5} \quad eV \qquad 1.4$$

where Z is the atomic number of the parent [8]. Parity, the total angular momentum and its projection along an axis must be conserved. Since the alpha particle has $J^{\pi} = 0^{+}$ the selection rules are simple. The orbital angular momentum, L, is restricted to values

$$|I_i - I_f| \leq L \leq |I_i + I_f| \qquad 1.5$$

where the subscripts refer to the initial and final states. If the parity of the initial and final states are the same, only even values of L are permitted and if the parities are different, L must be odd.

Mang derives a formula that expresses the decay constant in terms of the nuclear wave functions as follows [10]. The decaying system is described by a wave function $\Phi_J^M(X_1,..,X_A,t)$ which depends upon the spin and space coordinates of the A nucleons. It is assumed that the time development of this function in a space-time domain is known. χ_α is assumed to be the internal wavefunction of the alpha particle and Ψ_j^m a set of internal wavefunctions of the daughter nucleus. The quantity $g_{jL}^J(R,t)$ specifies the probability that the initial state Φ_J^M contains an alpha particle and daughter nucleus with specified quantum numbers at a radius R and time t. It is defined as follows:

$$g^{J}_{jL}(R,t) = \left[\binom{N}{2}\binom{Z}{2}\right]^{\frac{1}{2}} \int \sum_{m} (LjmM-m \mid JM)\ Y^{m}_{L}(\theta,\phi)$$

$$x \Psi^{M-m}_{j}(\eta)\, \chi_{\alpha}(\xi)\, \Phi^{M\,*}_{J}(X_1,.....,X_A,t)\ d\eta\ d\xi\ d\omega \qquad 1.6$$

where R = relative distance between daughter nucleus and alpha,

$\omega = (\theta,\phi)$ = angular coordinates of the alpha particle in center of mass system,

η,ξ = internal coordinates of alpha and daughter nucleus respectively including spin coordinates,

J,j,L = angular momentum of parent, daughter, and alpha particle with respect to the daughter respectively.

Angular momentum is conserved by summing over m substates and including the Clebsch-Gordan coefficients. The binomial coefficients account for the fact that the wave functions are not completely antisymmetrized.

The condition that Φ^{M}_{J} describes a properly decaying state is that there is a space time region in which $g^{J}_{jL}(R,t)$ has an exponential time dependence and that for large R the amplitude $g^{J}_{jL}(R)$ has only outgoing waves. A crucial assumption in the derivation is that a radius R_o exists such that for $R>R_o$ the alpha-daughter nucleus interaction can be expressed by a potential $V(R)$, and for $R<R_o$ nuclear wave functions may be used to calculate the amplitudes g^{J}_{jL}.

Under these assumptions and using the WKB approximation and the continuity equation one is led to the expression for the decay constant in terms of the barrier penetrabilities, $P_L(E)$, and reduced widths, γ^{2}_{jJL}.

This expression is

$$\lambda = \frac{1}{\hbar} \sum_{jL} P_L(E)\, \gamma_{jJL}^2 \qquad 1.7$$

where $$\gamma_{jJL}^2 = \frac{\hbar^2 R_o}{2M} \left| g_{jL}^J(R_o) \right|^2 \qquad 1.8$$

and $$P_L(E) = 2R_o\, q(R_o) \exp\left(-2 \int_{R_o}^{r_o} q(r)\, dr \right) \qquad 1.9$$

with $$q(r) = \left(\frac{2M}{\hbar^2} \left[E - \frac{\hbar^2}{2M} \frac{(L+\frac{1}{2})^2}{r^2} - V(r) \right] \right)^{\frac{1}{2}} . \qquad 1.10$$

In these expressions, E is the kinetic energy of the alpha particle and r_o is the outer turning point. Both $P_L(E)$ and γ_{jJL}^2 depend on R_o, but their product is independent of R_o. The reduced width, γ_{jJL}^2, contains all the information dependent on nuclear properties in the alpha decay process.

In thermal neutron (n,α) reaction studies it has been customary to use an alternative definition by Rasmussen [11,12] of the reduced width, δ^2, which is independent of R_o and is defined as follows

$$\delta^2 = \frac{\lambda h}{P} \qquad 1.11$$

where the barrier penetrability, P, is obtained by calculating the WKB integral from the inner to outer classical turning points of the potential barrier which includes a Coulomb term, centrifugal term and a nuclear term. The method of calculation is described in Chapter III.

The success of the many body theory applied to the shell model

has been demonstrated by Mang and Rasmussen [13] in extensive studies of even-even spheroidal nuclei. Poggenberg [14] has examined many of the features of this formulation and in particular, the penetration of the alpha particle through an anisotropic potential barrier. He includes extensive calculations for alpha emitters in the actinide region.

The use of this theory to describe alpha decay from thermal neutron capture states is complicated by the fact that one does not know the wavefunction of the initial (capture) state, Φ^M_J. This will be discussed in Chapter VII.

While it has been possible to obtain good agreement between experimental and theoretical relative decay rates using the shell model or collective model to describe initial and final states there is still a large discrepancy in the absolute values of the decay constants. Wilkinson [15] suggested that a possible solution was to assume that the nuclear surface consists mainly of alpha particle clusters. Calculations of Harada [16] show that the peak of the alpha particle density appears at the nuclear surface and that configuration mixing reinforces the formation of surface alphas significantly. Bencze et al [17], however, conclude that the discrepancy can be removed by using a proper deep alpha-nucleus potential and an accurate method of calculating penetrabilities (ie not the WKB method).

Thermal neutron (n, α) reaction studies were undertaken to obtain information on the alpha decay process from excited states of nuclei. This reaction is described by means of a two step process. A compound nucleus is formed by the capture of a thermal neutron and the state

subsequently decays by alpha emission in competition with the more probable gamma decay mode. Calculations of thermal neutron (n,α) cross sections have been made by Griffioen [18] for many nuclides using the statistical model. The width for alpha decay, Γ_α, is estimated from the average level spacing, D, [19] to give

$$\Gamma_\alpha = \frac{D}{2\pi} P \qquad 1.12$$

where P is the penetrability. The cross section is then obtained from

$$\sigma_{n\alpha} = \frac{\Gamma_\alpha}{\Gamma_\gamma} \sigma_{n\gamma} \qquad 1.13$$

where Γ_γ and $\sigma_{n\gamma}$ are the radiation width for gamma decay and the thermal neutron capture cross section respectively. It is assumed that $\Gamma_\gamma \approx \Gamma_{total}$.

Thermal neutron (n,α) cross sections have been reported for many nuclides for $Z \leq 30$ [20] and for certain nuclides in the rare earth region, in particular ^{149}Sm, ^{147}Sm, and ^{143}Nd [1,2,21]. In the present investigation these last three nuclides have been studied by means of a novel instrument which is called an electrostatic particle guide. By means of this device, which is discussed in detail in Chapter II, detailed measurements have been made of fine structure which corresponds to alpha transitions from the capture state to levels in the daughter nucleus up to greater than 2 MeV excitation.

Cross sections and alpha energies are presented for each transition and as well, the alpha decay schemes for ^{146}Nd, ^{144}Nd and ^{140}Ce which are derived from alpha decay from the capture states of ^{150}Sm, ^{148}Sm, and ^{144}Nd respectively. Experimental reduced widths have been calculated and are discussed in terms of the previously described alpha decay theory.

CHAPTER II

ELECTROSTATIC PARTICLE GUIDE

2.1 Description of The Technique

The study of fine structure in the alpha spectrum from thermal neutron (n,α) reactions has been limited by experimental difficulties which arise mainly from two effects : the intense background radiations from the reactor which seriously decrease the energy resolution of alpha particle detectors located in regions of moderate flux (10^8 to 10^{10} neutrons/cm^2/sec) , and low energy tailing of alpha spectra due to sample thickness and the requirement of high counting geometry. It was to solve these problems that the system described here was developed. In the system, which we call an electrostatic particle guide, the solution is achieved by transporting the alpha particles from the high background region to a low background region where they are counted. The transport of charged particles and in particular high energy alpha particles (typically 10 MeV) over large distances is accomplished by capturing them into a spiral orbit about a negatively charged wire held axially in a long cylinder.

The qualitative features of charged particles in such a 1/r central force are well known. Waters[22], in an unpublished report, was the first to study electron trajectories in this type of logarithmic potential. Hooverman[23], independently, treated the same problem and gave the important features of the orbits. Herb, Pauly and Fisher[24] found that the long mean free paths of electrons injected into such a field could be used

to build an efficient high vacuum gauge. The idea of transporting charged reaction products from heavy ion reactions over long distances was considered by Ghiorso and coworkers[25] and they were able to demonstrate that the device indeed worked in this application.

The electrostatic particle guide is shown in Figure 1. It is an aluminum cylinder 6.3 meters long and 7.5 cm inside diameter with an axial nichrome wire supported at the target end by a thin strip of ceramic and at the detector end by a stud connected to the electrode of a specially constructed high voltage terminal. The supports were designed to minimize the number of particles intercepted. In a recent modification to increase the collection efficiency the wire was replaced by a stainless steel tube 6 mm in diameter. The cylinder is evacuated to 10^{-6} torr and the central electrode held at a potential of -30 kV to -50 kV . The target is located at one end deep inside the thermal column of a reactor. Particles emerge isotropically over 4π geometry and of those which enter the electrostatic field a small proportion (about 0.05%) achieve a stable orbit and are transported the length of the cylinder. Here they are stopped by a silicon surface barrier detector which is in the low background region outside the reactor wall. The small collection efficiciency is compensated for by using large area targets (~50 cm^2) and irradiating at a flux two orders of magnitude higher than what can be used when the detector is located close to the target. Combining these two effects we obtain an order of magnitude increase in intensity relative to 2π counting in lower flux positions. Because of the self collimating feature of the device alpha spectra of 30 keV FWHM have been obtained

FIGURE 1: Electrostatic Particle Guide

The main features of the electrostatic particle guide are shown. Schematic particle orbits are indicated.

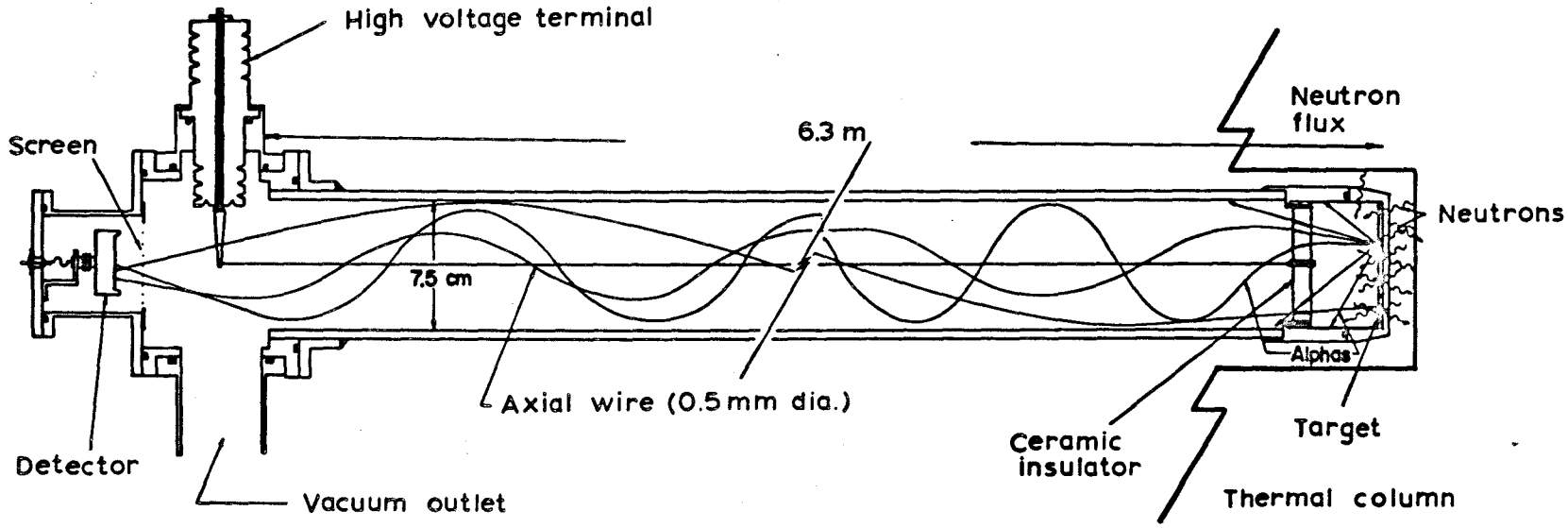
High voltage terminal
Screen
6.3 m
Neutron flux
Neutrons
7.5 cm
Alphas
Axial wire (0.5 mm dia.)
Ceramic insulator
Target
Detector
Vacuum outlet
Thermal column

with very little low energy tailing.

Stable operation has been maintained for long periods at -30 kV (greater than 500 hours) with no breakdown even in the intense radiation field of the thermal column. Some difficulty has been experienced at higher voltages. A current limiter, with ammeter, in series with the high voltage power supply output reduces intense RF discharges and provides a visual indication of high voltage breakdown. A high transmission screen is used to electrostatically shield and protect the detector. A 2000 gauss permanent magnet has been placed in front of the detector to deflect low energy electrons produced by field emission at the high voltage terminal. On occasion this effect has resulted in a factor of 10 increase in the RMS noise in the detector system without the magnet. A second, similar magnet is located about 50 cm from the detector to deflect away a current of positrons (produced presumably from pair production from high energy gamma rays near the reactor core) which are captured into a spiral orbit about the wire. The detector and source are at ground potential so there is no perturbation of the particle energy.

2.2 Collection Efficiency

2.2-1 Point Source Collection Efficiency

The collection efficiency for a point source which emits particles isotropically into 4π geometry is obtained by finding the fraction of these which achieve a bound orbit. These particles will traverse the length of the electrostatic particle guide to the detector end unless they strike the central electrode. A correction for those striking the wire is calculated in Section 2.2-3 .

The particle position in the electrostatic field between the central electrode and the outer cylinder is most conveniently expressed in cylindrical coordinates (r,Θ,z) where the z-axis coincides with the center of the wire. Consider (Figure 2) a particle with velocity, v_a, and charge, q, injected into the field from a point source at a radius r_o, with initial conditions determined from the angles β and ϕ. The component of velocity v_z parallel to the wire transports the particle down the cylinder to the detector. Since this component is constant it is ignored in what follows and the particle motion in a plane (r,Θ) perpendicular to the z axis is considered. The component v_p in this plane leads to spiral motion about the wire. Now

$$v_p = v_a \sin\beta \doteq v_a \beta \qquad \text{for small } \beta . \qquad 2.1$$

The particle energy in this plane is then $E_\perp$ where

$$E_\perp = m\dot{r}^2/2 + mr^2\dot{\Theta}^2/2 + V(r) \quad . \qquad 2.2$$

At $t = 0$, this takes the form

$$E_\perp = E_a \beta^2 + V(r_o) \qquad 2.3$$

where E_a is the total kinetic energy of the particle and m is its mass. The potential energy term, $V(r)$, for two concentric cylinders is given by

$$V(r) = - |qV_o| \frac{\ln(r/R)}{\ln(s/R)} \qquad 2.4$$

where V_o is the potential difference between the two cylinders,

R is the radius of the outer cylinder,

s is the radius of the inner cylinder.

FIGURE 2: Definition of Particle Coordinates

Cylindrical coordinates (r,θ,z) are used to define the particle position at a time, t . The angles β and ϕ , and r_o , define the initial conditions.

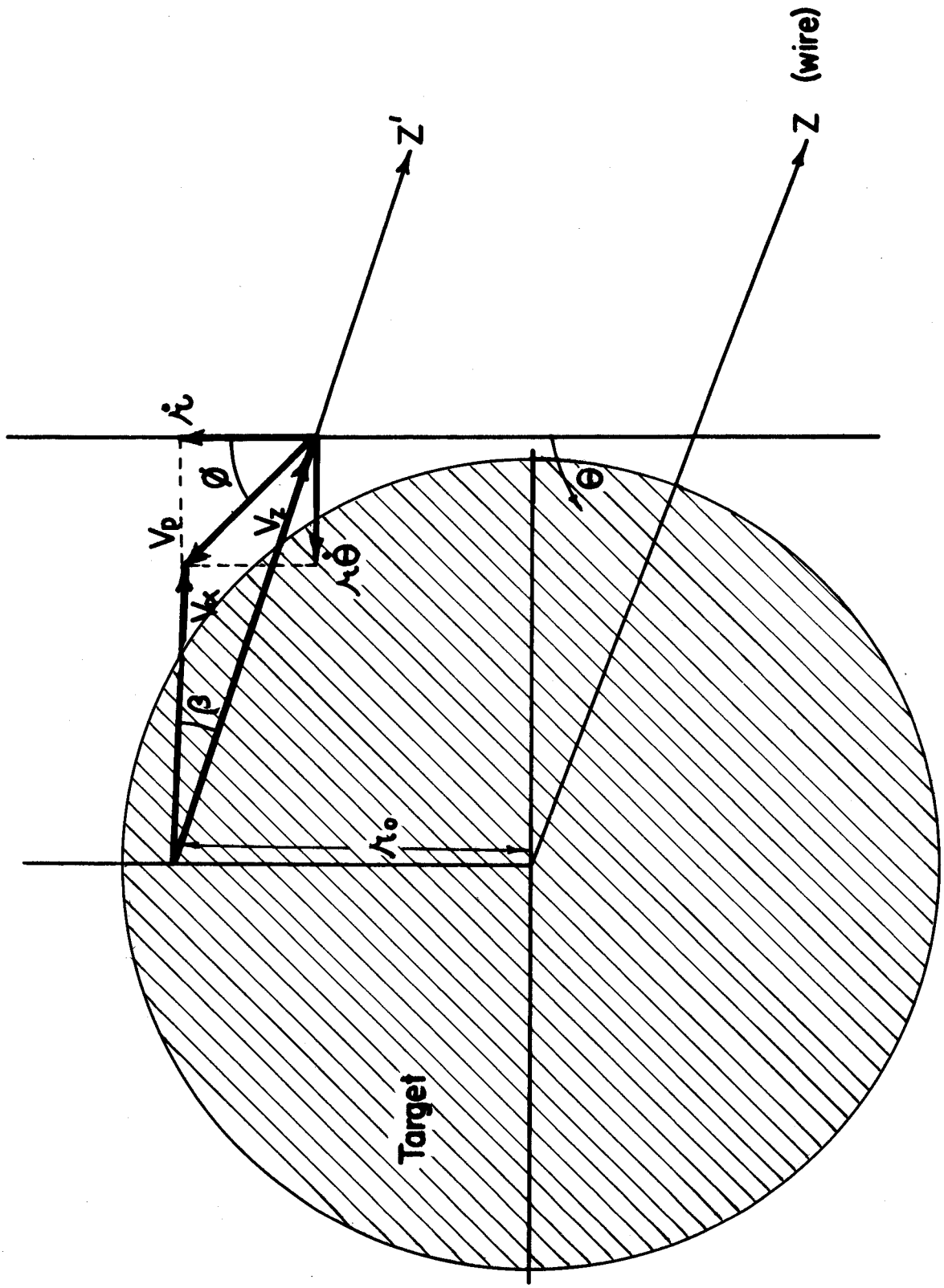
Z (wire)
Z'
ṙ
ø
Vp
Vr
rθ̇
Vk
β
r₀
θ
Target

It is convenient to eliminate $\dot{\theta}$ from equation (2.2) by expressing $\frac{1}{2}mr^2\dot{\theta}^2$ in terms of the initial conditions using the conservation of angular momentum L. Thus

$$L = mr^2\dot{\theta} = mr_o^2\dot{\theta}_o = mr_o v_p \sin\phi \quad . \tag{2.5}$$

Using this we obtain

$$\tfrac{1}{2}mr^2\dot{\theta}^2 = \tfrac{1}{2}L^2/mr^2 = \tfrac{1}{2}mv_a^2\,\beta^2\sin^2\phi\; r_o^2/r^2 = E_a\,\beta^2\sin^2\phi\; r_o^2/r^2 \quad . \tag{2.6}$$

At an apogee or perigee, $\dot{r} = 0$. Thus equation (2.2) at apogee when combined with equations (2.3) and (2.6) reduces to

$$E_\perp = E_a\beta^2 + V(r_o) = E_a\beta^2\sin^2\phi\,\frac{r_o^2}{r_{max}^2} + V(r_{max}) \tag{2.7}$$

For a given value of r_o , the largest β is determined when the apogee (r_{max}) is equal to R . When $r_{max} = R$, $\beta = \beta_{max}$, $V(R) = 0$ and one obtains

$$\beta_{max}^2 = \frac{|qV_o|}{E_a}\frac{\ln(r_o/R)}{\ln(s/R)}\,(1 - (r_o/R)^2\sin^2\phi\,)^{-1} \quad . \tag{2.8}$$

The value of β_{max} determines the size of the "acceptance cone" for a given r_o . The collection efficiency, $F(r_o)$, for a point source is then given by the solid angle of the acceptance cone divided by 4π . Thus

$$F(r_o) = \frac{1}{8\pi}\int_0^2 \beta_{max}^2\, d\phi = \frac{|qV_o|}{4E_a}\frac{\ln(r_o/R)}{\ln(s/R)}\,(1 - r_o^2/R^2)^{-\frac{1}{2}} \quad . \tag{2.9}$$

Examination of equations (2.8) and (2.9) reveals some interesting features. The solid angle of the acceptance cone decreases as r_o

increases. At a particular radius the angle of the acceptance cone, β_{max}, is greatest for $\phi = \pi/2$ which corresponds to the maximum amount of angular momentum with which the particle can be injected.

Using equation (2.9) the fraction of particles collected as a function of the distance of the point source from the wire was calculated for the particles emitted in the $^{6}Li\ (n,\alpha)\ ^{3}T$ reaction. The results of these calculations are shown in Figure 3. The collection efficiency, as shown in equation (2.9), varies directly with the charge of the particle and inversely with its energy. Thus the collection efficiency for the 2.74 MeV triton is a little less than half that for the 2.05 MeV alpha particle.

2.2-2 Extended Source Collection Efficiency

Large area targets are used to increase the total number of particles that achieve a bound orbit around the wire. Targets as large as the area of the tube can be used effectively because (as shown in Figure 3) the collection efficiency diminishes to zero only when r_o equals the radius of the tube.

The collection efficiency for an extended uniform target can be readily calculated from equation (2.9) by averaging over the area of the target. Thus for a target of radius b, the collection efficiency, F_c, is given by

$$F_c = \frac{2\int_s^b F(r_o)\, r_o\, dr_o}{(b^2 - s^2)}$$

$$= \frac{|qV_o|R^2}{2E_a \ln(s/R)(b^2 - s^2)} \left[x(1 - \ln(b/R)) - \ln((1 + x)R/b) - y(1 - \ln(s/R)) + \ln((1 + y)R/s) \right] \qquad 2.10$$

FIGURE 3: Fraction of Particles Collected

The fraction of particles collected for a point source at a radius r_o , $F(r_o)$, is shown plotted versus r_o . The calculations were made for the alpha and triton from the $^{6}Li\ (n, \alpha)^{3}T$ reaction using $R = 3.75$ cm , $s = 0.025$ cm and $V_o = 30$ kV .

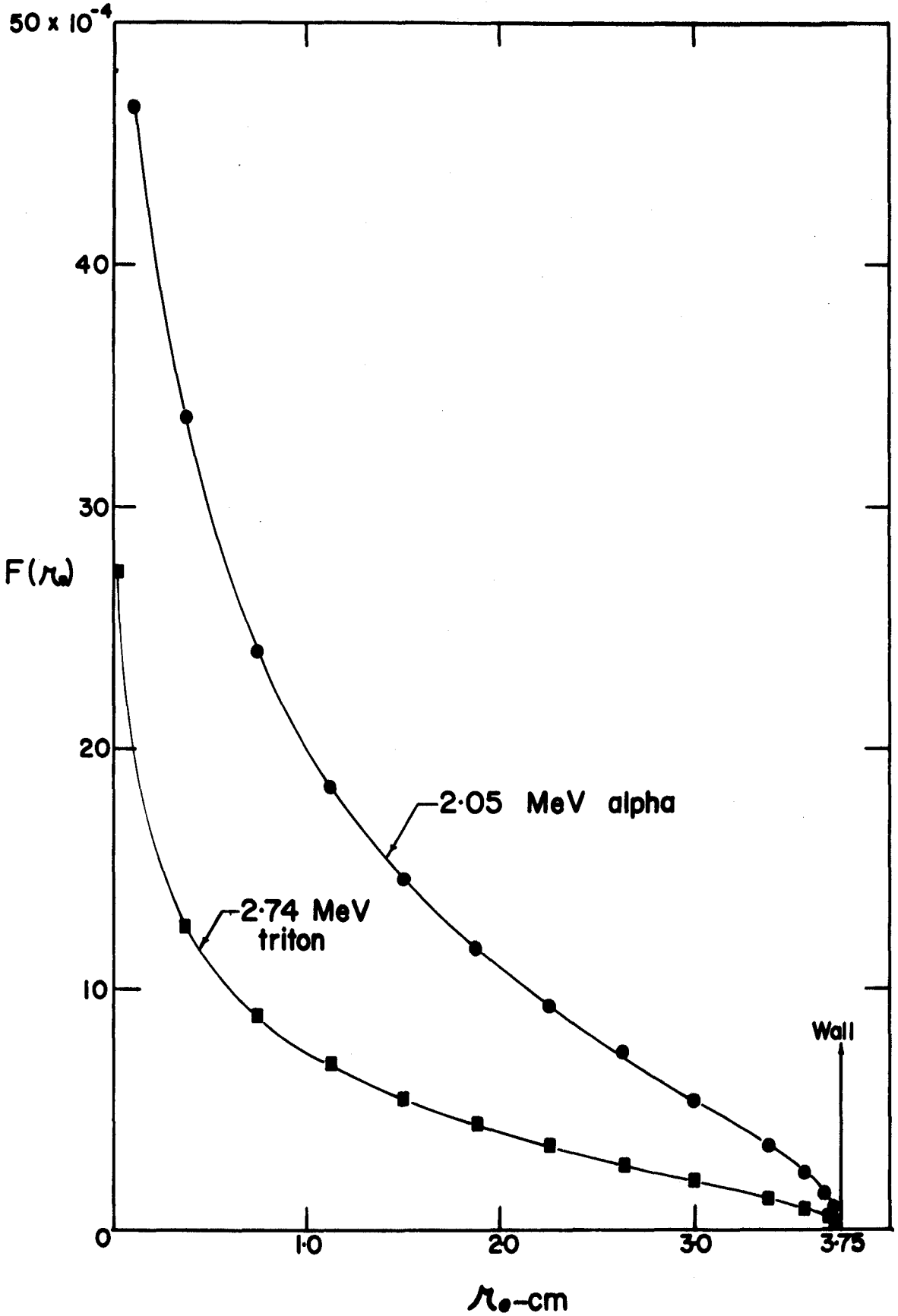
50 x 10⁻⁴
40
30
20
10
0
F(ρ)
2·05 MeV alpha
2·74 MeV
triton
Wall
1·0
2·0
3·0
3·75
ρ₀-cm

where $x = (1 - (b/R)^2)^{\frac{1}{2}}$ and $y = (1 - (s/R)^2)^{\frac{1}{2}}$. For $b \gg s$ and $R \gg s$ this reduces to

$$F_c = \frac{|qV_o| R^2}{2E_a \ln(s/R) b^2} \left[x(1 - \ln(b/R)) - \ln((1 - x)R/b) - (\ln(2) - 1) \right] . \qquad 2.11$$

In the case when the target radius is equal to the tube radius ($b = R$) equation (2.11) reduces to

$$F_c = \frac{(\ln(2) - 1)|qV_o|}{E_a \ln(R/s)} . \qquad 2.12$$

This is the basic relationship which determines the fraction of particles emitted by an extended source that achieves a bound orbit. Most of these are transported the length of the tube without loss. There are, however, a small number which achieve a bound orbit but are lost. This effect is discussed in the next section.

2.2-3 Particles Striking the Wire

If the perigee or minimum radius (r_{min}) for a particle which enters a bound orbit is less than the radius of the central wire, the particle strikes the wire and is lost. Thus, a particle injected at an angle β from a point at a radius r_o requires at least a minimum angular momentum so that $r_{min} \geq s$. At a perigee, $\dot{r} = 0$, $r = r_{min}$ and one obtains an equation identical to (2.7) with r_{max} replaced by r_{min} ,

$$E_a\beta^2 - |qV_o| \frac{\ln(r_o/R)}{\ln(s/R)} = E_a\beta^2 \sin^2\phi \, r_o^2/r_{min}^2 - |qV_o| \frac{\ln(r_{min}/R)}{\ln(s/R)} .$$

2.13

Using this equation, the minimum value of ϕ , below which the particle hits the wire, is obtained by setting $r_{min} = s$. Thus,

$$\phi_{min} = \sin^{-1}\left[\frac{s}{r_o}\sqrt{1 + \frac{|qV_o|}{E_a\beta^2}\frac{\ln(s/r_o)}{\ln(s/R)}}\right] \quad . \qquad 2.14$$

The solid angle, $A_w(r_o)$, lost to particles striking the wire is given approximately by

$$A_w(r_o) = 4\int_0^{\beta_{max}(\phi=0)} \phi_{min}\,\beta\,d\beta \qquad 2.15$$

under the conditions that $R \gg s$ and r_o is greater than about $10s$. Expressing ϕ_{min} in terms of β using equation (2.14) yields on integration the fraction of particles from a point source which strike the wire:

$$A_w(r_o) = A_w(r_o)/4\pi$$

$$= \frac{s|qV_o|}{2\pi r_o E_a}\left[\frac{\sqrt{\ln(R/r_o)}}{\sqrt{\ln(R/s)}} + \frac{\ln(r_o/s)}{\ln(R/s)}\ln\left\{\frac{\sqrt{\ln(R/r_o)} + \sqrt{\ln(R/s)}}{\sqrt{\ln(r_o/s)}}\right\}\right] . \qquad 2.16$$

An exact expression for $F_w(r_o)$ is derived in Appendix I. For an extended source of radius b , the fraction of particles which strike the wire is given by

$$F_w = \frac{2}{(b^2 - s^2)}\int_s^b F_w(r_o)\, r_o\, dr_o \quad . \qquad 2.17$$

For a particular size of target the correction factor for particles lost to the wire is conveniently expressed as the ratio of the fraction of particles which strike the wire, equation (2.17), to the fraction of particles which achieve a bound orbit, equation (2.10) :

$$R_h = F_w / F_c \quad . \qquad 2.18$$

Evaluating this expression for a target radius equal to the radius of the tube ($b = R$) for $R = 3.75$ cm and $s = 0.025$ cm (the values used in the initial experiments) gives $R_h = 0.05$ so that the collection efficiency, F_c, should be multiplied by 0.95 to account for this effect for the particular choice of R and s.

2.2-4 Determination of the Optimum Wire Radius

An examination of equation (2.12) for the collection efficiency, Fc, reveals that for a particular outer radius, R, and target radius, b, the number of particles collected increases as the wire radius, s, increases. It is also evident from equation (2.16) that the number of particles striking the wire also increases. The number of particles entering a bound orbit per second is

$$N_c = \pi (R^2 - s^2) N_o F_c \qquad 2.19$$

where F_c is given by equation (2.10) and N_o is the number of particles emitted at the source per unit area per second. Similarily, the number of particles which strike the wire per second is given by

$$N_w = \pi (R^2 - s^2) N_o F_w \qquad 2.20$$

where F_w is given by equation (2.17). Since the approximations used in the previous section to derive equation (2.16) for $F_w(r_o)$ are not valid for large s, it is necessary to use equation (A1.12) of Appendix I in this calculation.

The total number of particles that are collected is then given by

$$N_t = N_c - N_w \quad . \qquad 2.21$$

This quantity was determined by calculating N_c from equation (2.19) and determining N_w by numerically integrating $R(r_o)$ to obtain F_w. This was done for $R = 3.75$ cm and for values of s between 0.025 cm and 3.2 cm. N_o was chosen to be 100 particles/cm^2/sec and the calculations were performed for a 5.0 MeV alpha particle with V_o equal to 30 kV. The results are shown in Figure 4, in which the number of particles collected per second is plotted versus the radius of the wire, s. The ratio, R_h, is also plotted on the same graph.

An examination of these curves reveals that the highest count rate is obtained for a wire radius of 0.3 cm where 34.2% of the alpha particles which achieve a bound orbit strike the wire. The ratio of the count rate at the maximum to the rate for a 0.025 cm radius wire is 1.33. For a wire radius of 0.025 cm, voltage breakdown is a problem above 25 kV. With a central electrode 0.3 cm in radius it has been possible to maintain stability at 45 kV to 50 kV. Thus, by increasing the radius from 0.025 cm to 0.3 cm a 33% gain is realized by optimizing s. In addition there is a factor of two increase due to the increased voltage giving an overall increase of about 2.6.

2.2-5 Comparison of Calculation with Experiment

The experimental collection efficiency was measured for the products of the reaction $^6Li\ (n,\alpha)\ ^3T$. A target of ^6Li was prepared by electrodeposition on a backing 3.75 cm in radius. The target was placed in one end of the instrument, as shown in Figure 1, and inserted into the thermal column of the reactor. The total intensities of the 2.05 MeV

FIGURE 4: Determination of Optimum s

The number of particles collected, N_t , and the fraction of particles lost, R_h , are shown plotted versus the wire radius s . The calculations were performed for a 5.0 MeV alpha particle with V_o equal to 30 kV and for an outer radius equal to 3.75 cm.

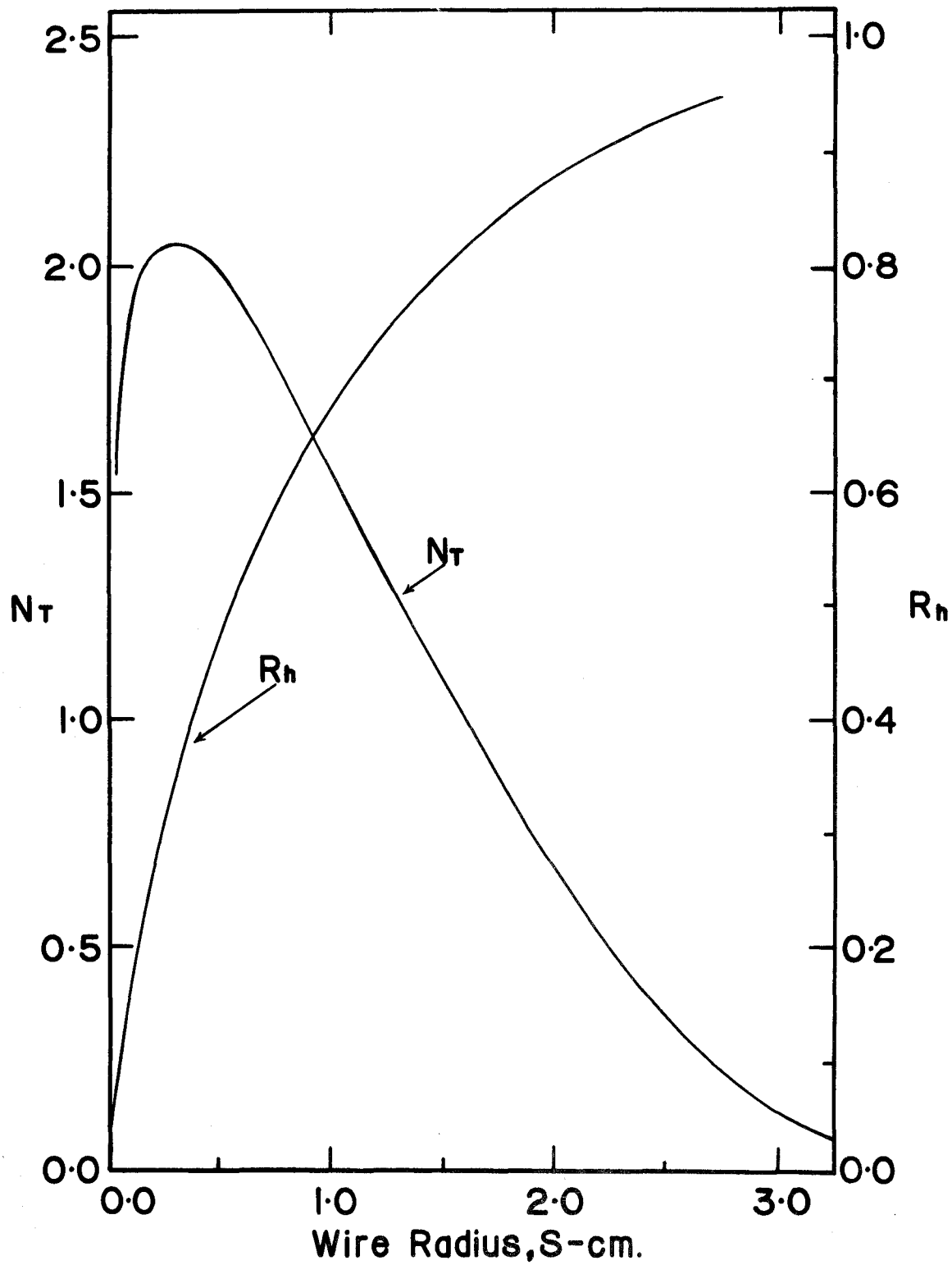
2·5
2·0
1·5
1·0
0·5
0·0
1·0
0·8
0·6
0·4
0·2
0·0
NT
Rh
NT
Rh
0·0
1·0
2·0
3·0
Wire Radius, S-cm.

alpha and 2.74 MeV triton groups emerging from the tube at the detector end were measured as a function of the voltage on the wire. Sufficient ^6Li was present that a particle energy spectrum could be obtained with the detector 6.3 meters from the target and no voltage on the wire. The 2.05 MeV alpha particle intensity increased two orders of magnitude when 30 kV was applied to the wire. This increase is equivalent to moving the detector to within 0.63 meters of the target. The enhancement factor of the intensities of the alpha and triton groups was measured at several voltages and these data are shown in Figure 5 . The results are expressed in terms of the ratio of the measured intensity at a given voltage to the intensity at zero volts, N_V/N_O . The solid lines represent theoretical collection efficiencies calculated using equation (2.11) and correcting for the fraction of particles hitting the wire. The linear relationship between V_O and N_V/N_O predicted by equation (2.11) is verified experimentally for both the alpha and triton groups. The measured values are in good agreement with the calculations for the triton group. The results for the alpha group are alsc quite satisfactory although there appears to be a small but systematic departure from the theoretical curve at higher voltages. This deviation represents a loss of particles which is possibly due to deviations from ideal conditions such as imperfect alignment of the central wire, residual gas pressure, or effects due to the wire supports. A part of the discrepancy is certainly due to the divergence of the charged particle beam between the end of the tube and the detector (about 15 cm). In the measurement of N_V/N_O particles that reached the detector at a distance from the axis greater than R were not

FIGURE 5: Intensity Enhancement Factor

The variation of the intensity enhancement factor (N_V/N_O) is shown plotted versus the voltage on the central wire, V_O , for the products of the $^{6}Li\ (n,\alpha)\ ^{3}T$ reaction. The calculated values are shown as a line and are compared with the measured values ($\updownarrow$) .

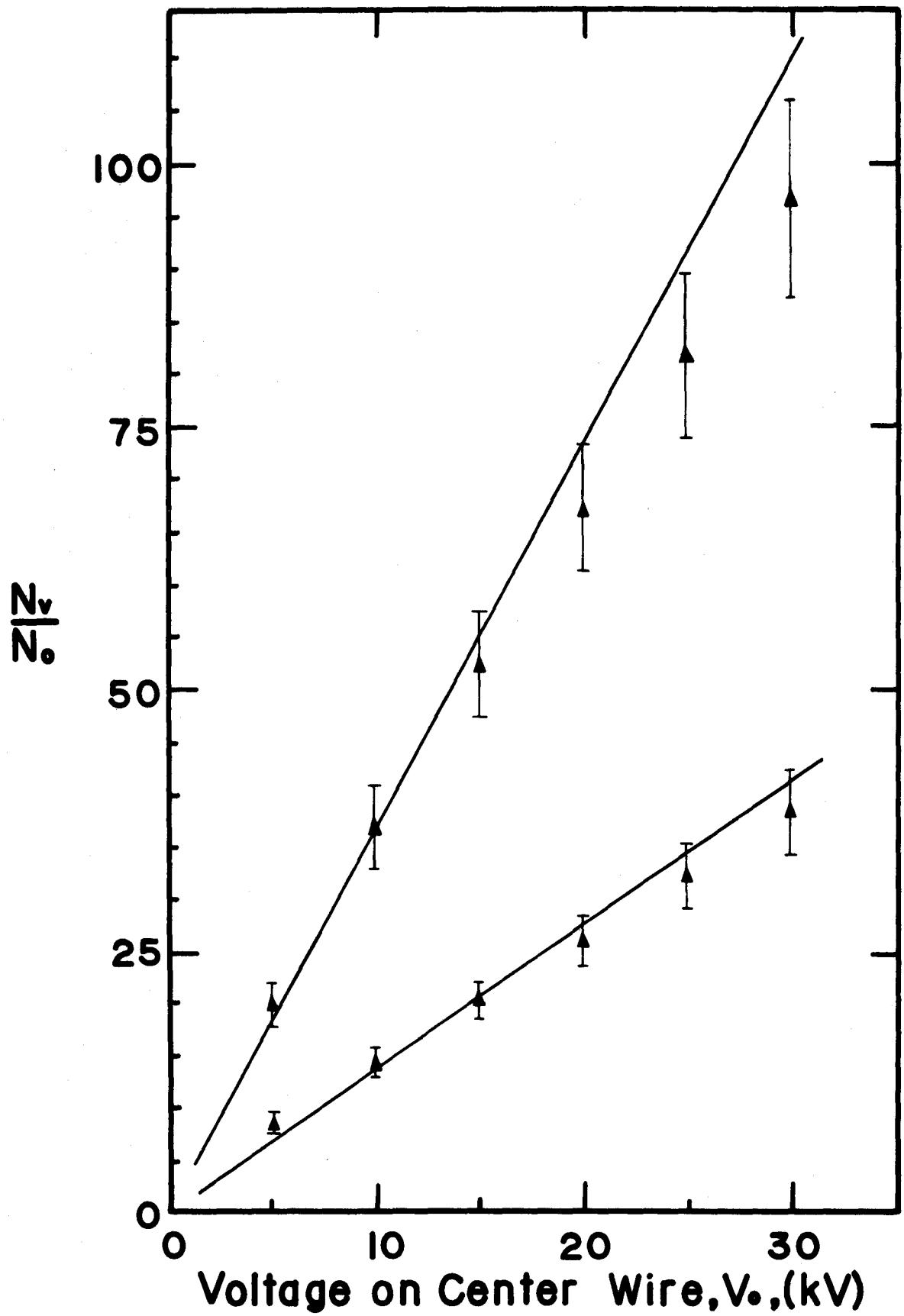
100
75
50
25
0
$\frac{N_v}{N_o}$
0
10
20
30
Voltage on Center Wire, V_o, (kV)

recorded. A correction for these would give better agreement.

The good agreement between the experimental results and the theory demonstrates that equation (2.11) can be used to calculate meaningful collection efficiencies as a function of the basic parameters of the electrostatic particle guide.

The installation of a central electrode 0.3 cm in radius gave about two thirds of the calculated increase in collection efficiency (or about the same efficiency as the 0.025 cm wire at the same voltage). The difficulty of supporting the six meter long tube in an axial position in exact alignment is one of the major reasons for this discrepancy. The higher collection efficiency due to the increased operating voltage has, however, justified this modification.

2.3 Particle Orbits and Radial Distribution

2.3-1 Calculation of Orbits

In the course of studying the collection efficiency of this device, it became clear that when large area targets were used, the intensity of particles emerging was not uniform and appeared greater near the wire. Further, when point source targets and small area detectors were used, large oscillations in particle intensities were observed as a function of wire voltage. This was most dramatic in the $^{6}Li\ (n,\alpha)\ ^{3}T$ spectrum where the alpha and triton intensities oscillated out of phase with each other as the voltage was varied. It seemed that these features might have some importance in experiments planned for the future so it was decided to investigate theoretically the properties of the individual trajectories.

Hooverman[23] treated the problem of the shape of electron orbits in a logarithmic potential for various input parameters by numerically integrating $\theta(r)$ and $t(r)$ from apogee to perigee to obtain the angular and temporal separation between successive apogees and perigees. Knowing the corresponding radii for apogee and perigee he was able to sketch the orbits quite accurately.

To obtain more information, however, it is desirable to be able to calculate the instantaneous radius r, and position angle θ, as a function of time. These functions cannot be obtained explicitly but can be determined by numerical techniques. The equations of motion are readily obtained from the Lagrangian written terms of the parameters of our system. Thus,

$$\ddot{r} = A_1/r^3 + A_2/r \qquad 2.22$$

and

$$\dot{\theta} = C/r^2 \quad , \qquad 2.23$$

where

$$A_1 = r_o^2 v_p^2 \sin^2\phi \quad , \qquad 2.24$$

$$A_2 = (|qV_o|)/ m \ln(s/R) \quad , \qquad 2.25$$

and

$$C = A_1^{\frac{1}{2}} \quad . \qquad 2.26$$

At $t = 0$, $r = r_o$, $\dot{r} = v_p \cos\phi$, and $\theta = 0$. The differential equations (2.22) and (2.23) were solved, subject to the initial conditions, by digital-analogue techniques using a simulated analogue computer program, MIMIC [50], written for a digital computer. With this program r and θ can be obtained for any desired value of t. Details of the method of calculation are given in Appendix II. Some sample orbits for

2.74 MeV tritons are shown in Figure 6 . Points were calculated at 4.7 nanosecond intervals. The time of flight for a 2.74 MeV triton is 471 nanoseconds so that about 50% of the length of the trajectory is represented in Figure 6 . Three orbits are shown for particles originating at a distance of 1 cm from the wire but with different values of β and ϕ . Typically, a particle will make several spiral orbits before emerging from the other end of the tube.

2.3-2 Calculation and Measurement of the Radial Distribution at the Detector End

The particle radial distribution at the exit end of the particle guide was first calculated for a point source at a radius r_o . This was done by calculating the position coordinates, r and θ , at the instant the particle emerges from the end of the tube for many values of β and ϕ representing equal amounts of solid angle over the acceptance cone. Approximately 180 trajectories were included in the calculation. These results were summed to obtain the particle radial distribution at the exit end for a point source at the other end.

To obtain the density distribution for an extended source (b = R) the calculation was repeated by varying r_o from 0.5 cm to 3.5 cm in 0.5 cm increments. The total radial density distribution function (now involving about 1300 trajectories) was then obtained by summing the contributions from each increment of the source area weighted by the point source collection efficiency function (equation 2.9), and correcting for particles that strike the wire.

Using the calculated density distribution function, and knowing the intensity of the 2.74 MeV triton group at zero volts, the absolute

FIGURE 6: Calculated Trajectories

The calculated trajectories of 2.74 MeV tritons for various initial conditions are shown in polar coordinates (r,θ): No. 1) $\beta = 0.0143$ rad, $\phi = 0.393$ rad; No. 2) $\beta = 0.0202$ rad, $\phi = 0.393$ rad ; No. 3) $\beta = 0.0202$ rad, $\phi = 1.021$ rad . The cross section of the center wire with the appropriate radius is represented by the black circle in the middle.

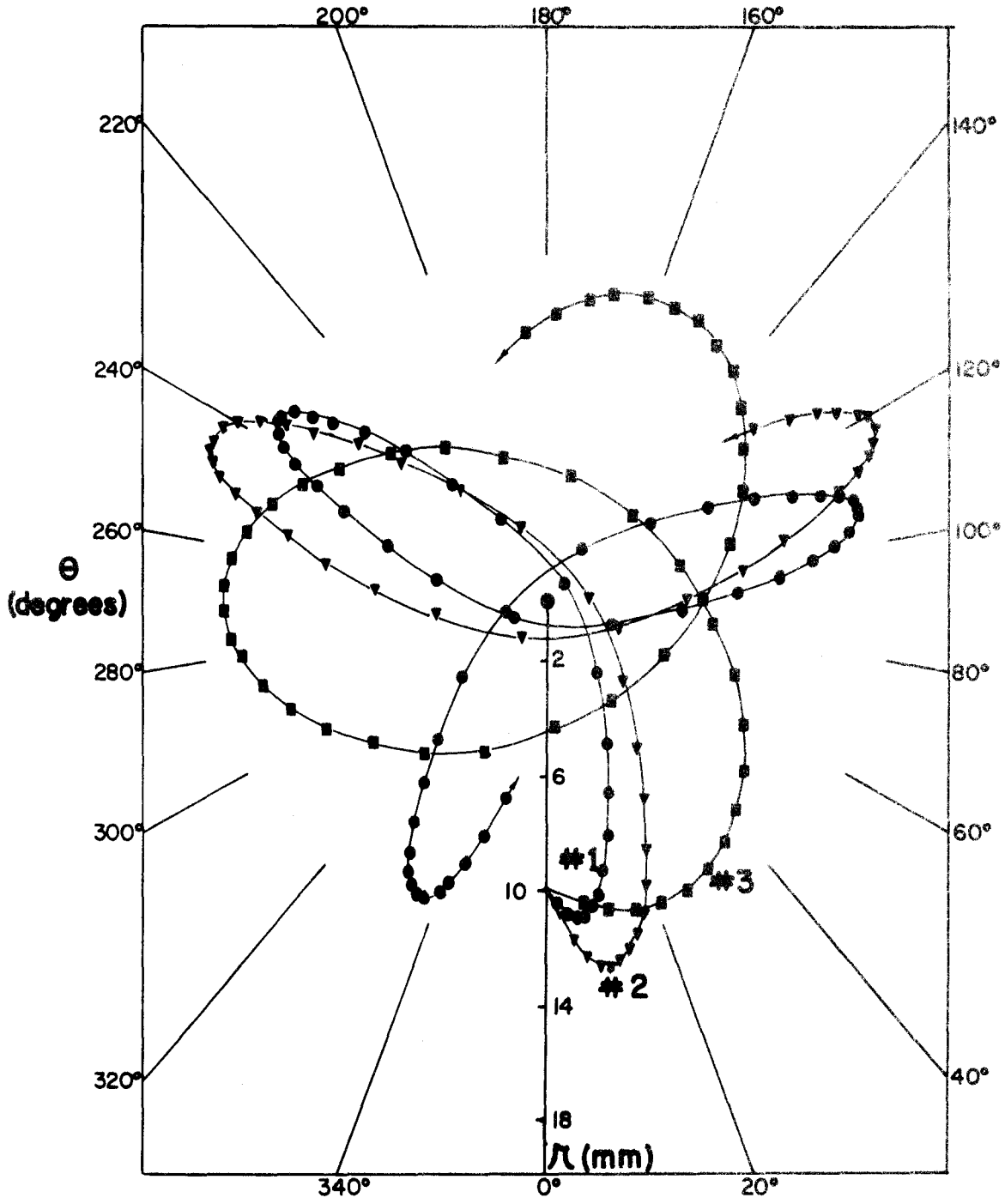
200°
180°
160°
220°
140°
240°
120°
260°
100°
Θ
(degrees)
280°
80°
300°
60°
320°
40°
340°
0°
20°
2
6
10
14
18
#1
#2
#3
r (mm)

particle densities were calculated as a function of the radial distance from the center wire at the detector end. The resuls of these calculations is shown in Figure 7 . The particle density was then measured experimentally at four different radii and compared with the calculations. These results have been plotted with the thecretical curve shown in Figure 7 . The agreement is very good.

The results show that a small area detector located on the axis of the cylinder is intercepting the region of highest particle density. Also, if a larger detector is used the intensity will not increase in an amount proportional to the increase in area of the detector.

FIGURE 7: Radial Density Function

The calculated (⧳) and experimental (⧳) values of the particle density is plotted versus the radial distance from the wire at the detector end of the particle guide. The calculations were made for a 2.74 MeV triton and a wire voltage of 20 kV .

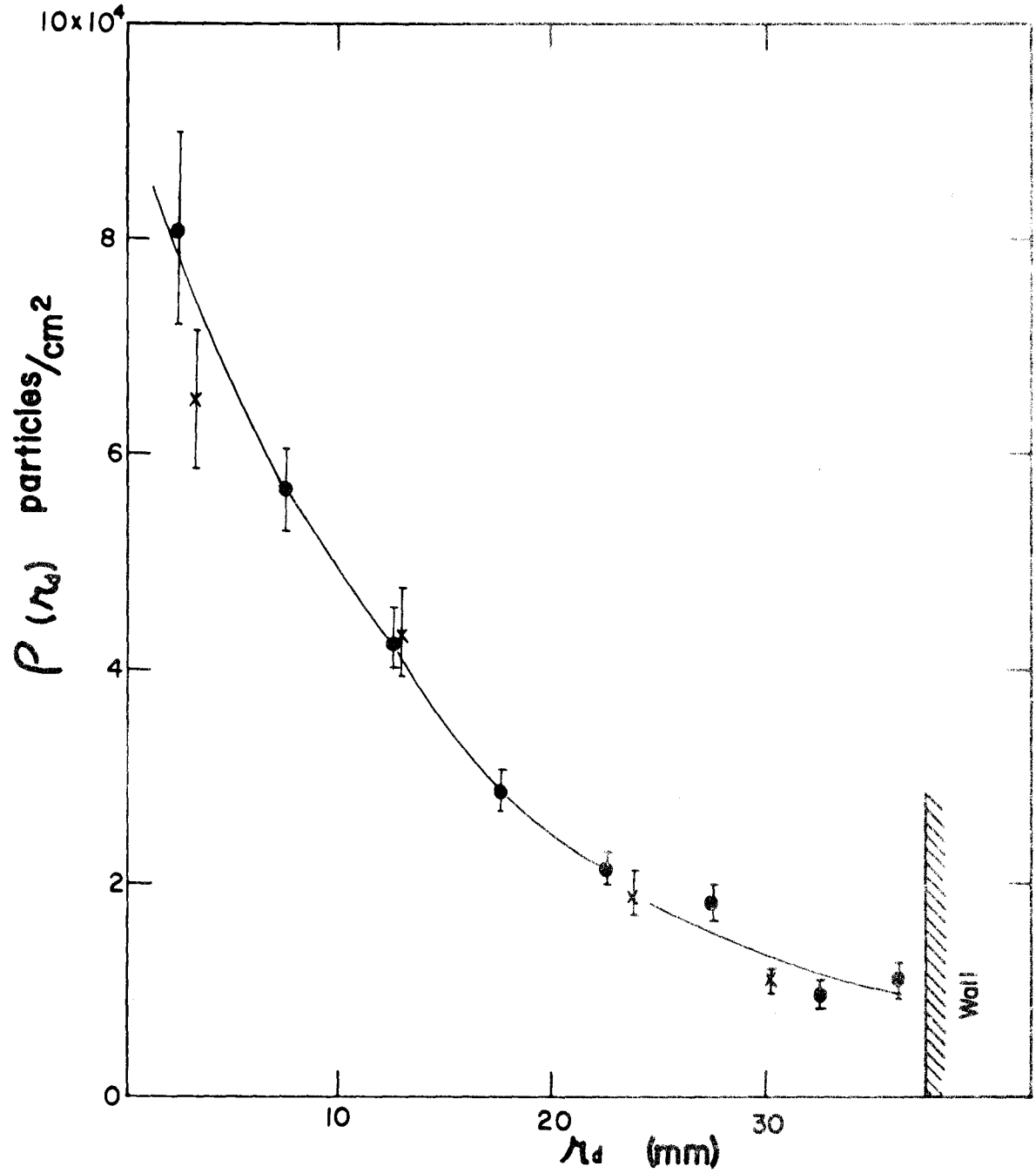
10x10⁴
8
6
4
2
0
ρ (r_d) particles/cm²
10
20
30
r_d (mm)
Wall

CHAPTER III

EXPERIMENTAL DETAILS AND DATA ANALYSIS

3.1 Sample Preparation

Large area circular targets with a diameter of 7.5 cm were prepared by electrodeposition. Samples of neodymium and samarium in the oxide form enriched to more than 90% in the isotope of interest were obtained from Oak Ridge National Laboratory. The sample was dissolved in nitric acid and evaporated to dryness to convert the material to the nitrate form. The nitrate was then disolved in water (about 0.1 ml per mg of sample), mixed with 150 ml of 2-Propanol, and electrodeposited onto a polished aluminum disk 7.5 cm in diameter and 1 mm thick. The plating cell is shown in Figure 8 . It was found that by turning the platinum electrode slowly (about 1 RPM) and by using about 300 volts, uniform targets could be obtained with essentially 100% plating efficiency. The target was heated to decompose the electrodeposited material to its oxide form to minimize the target thickness. Targets typically contained 2 to 5 mg of enriched isotope.

3.2 Counting Technique

To obtain data on the thermal neutron (n, α) reaction for a particular nuclide, the target was placed in the electrostatic particle guide as indicated in Figure 1 . The assembly was evacuated and placed in the thermal column of the McMaster reactor at a flux position of 10^{10} neutrons/cm^2/sec. With about -30 kV on the central electrode the spectrum was

FIGURE 8: Plating Cell

The plating cell used to prepare large area targets for the electrostatic particle guide is shown.

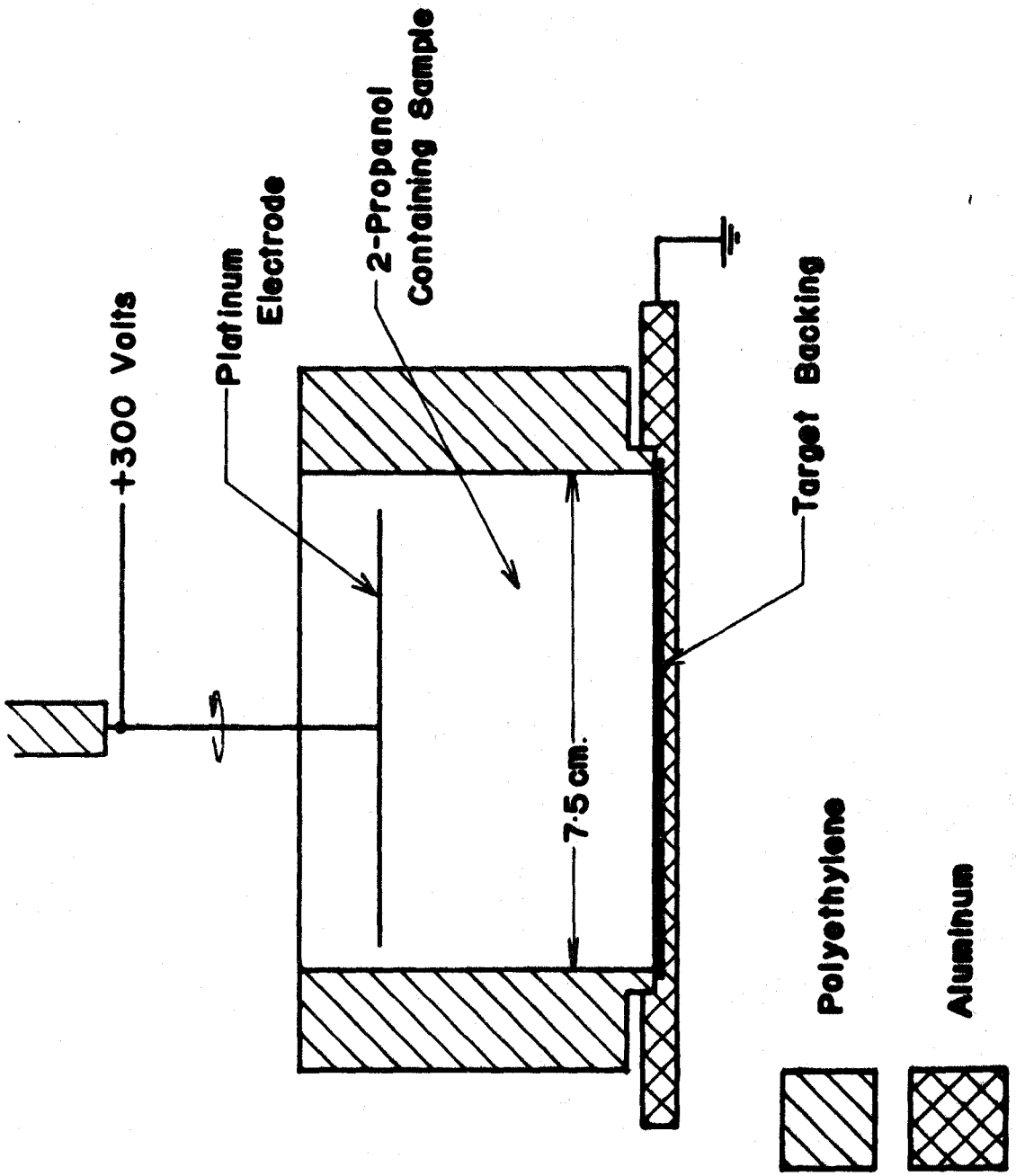
+300 Volts
Platinum Electrode
2-Propanol Containing Sample
Target Backing
7.5 cm.
Polyethylene
Aluminum

obtained by measuring the alpha particles with a 3 cm^2 surface barrier detector placed near the axis. An ORTEC 101-201 preamplifier and amplifier system was used and the data analyzed and recorded in a 400-channel pulse height analyzer. Since it required many days to accumulate sufficient statistics the analyzer memory was printed out daily to prevent the loss of more than one day's data in the event of equipment failure. Gain shift amounted to less than two channels (20 keV) over a month long experiment and the spectra were corrected for this shift.

A canned bismuth plug was placed in front of the particle guide to reduce the gamma field at the detector. This lowered the measured background by a factor of ten to a level about equal to that with the reactor off.

The spectrum of the $^{149}Sm(n, \alpha)\ ^{146}Nd$ reaction was obtained with a 0.05 cm diameter axial wire while the $^{143}Nd\ (n, \alpha)\ ^{140}Ce$ and $^{147}Sm\ (n, \alpha)\ ^{144}Nd$ reactions were measured with a 0.6 cm diameter axial electrode.

3.3 Spectrum Analysis

The measured alpha spectra were analyzed to obtain alpha energies and cross sections. From the energies the Q-values were obtained and hence the level scheme of the daughter nucleus. Both the Q-values and cross sections were used to determine the experimental reduced widths described in the next section.

Because of the self-collimating feature of the electrostatic particle guide and because thin targets (50 to 100 micrograms/cm^2) were used, the peaks in the spectrum were very nearly Gaussian in shape. For

this reason the peak positions were determined by fitting a Gaussian to the data in the vicinity of the peak channel. This was done by means of a standard non-linear least squares technique[26] and a program written for the IBM 7040 computer. The alpha energies were then determined by using a calibration curve obtained using alpha energy standards.

The calibration curve was obtained by determining the linearity of the electronic system by means of a mercury pulser and the accurately known alpha energies of the ^{228}Th decay chain[27]. In the ^{149}Sm and ^{147}Sm experiments the 8.734± 0.003 MeV peak [28] from the ^{149}Sm(n,α)^{146}Nd was used as a normalization point for the energy scale. The peak at 9.443± 0.003 MeV [28] was used for the same purpose in the fine structure studies of the ^{144}Nd(n, α) ^{140}Ce reaction. This technique of normalizing to well-known peaks in the spectrum on the reaction under investigation was adopted to prevent contamination of the system by recoils from the ^{228}Th source which could cause background problems.

The Q-value, corresponding to an alpha transition of energy E_a , is given by

$$Q_a = E_a (1 - m_a/M_d) \qquad 3.1$$

where m_a is the alpha particle mass and M_d is the mass of the daughter nucleus. To determine the excitation energy the Q-value for decay to the excited state was subtracted from the Q-value for the decay to the ground state to give the excitation energy, E_x ,

$$E_x = Q_{a,g.s.} - Q_{a,x} \qquad 3.2$$

Relative cross sections of the various peaks in the fine structure spectrum were obtained as follows. The number of events in each peak, $R_m(E)$, was determined by numerical integration. This value was corrected for the energy dependence of the collection efficiency for the particle guide to obtain the true number of events, $R_t(E)$. The relative cross section of a peak at energy E_1 to one at energy E_2 is then given by the formula

$$\frac{R_t(E_1)}{R_t(E_2)} = \frac{E_1}{E_2}\frac{R_m(E_1)}{R_m(E_2)} \qquad 3.3$$

where the energy correction factor, E_2/E_1 , is obtained from the collection efficiency formula, equation(2.12).

The effective thermal neutron (n,α) cross sections, $\hat{\sigma}_{n\alpha}$, for the fine structure spectra were obtained by normalizing the relative cross sections to the known values for the most intense alpha transitions to the ground state or first excited state of the daughter nucleus which have been determined by Beg (28) for ^{149}Sm, ^{147}Sm and ^{143}Nd.

The validity of the energy correction for a small detector which does not cover the whole end area of the electrostatic particle guide was investigated experimentally by studying the spectrum from a large area ^{226}Ra source. The values, $R_m(E)$, were obtained using the electrostatic particle guide and the values, $R_t(E)$, were obtained by placing the source near the detector. The quantity

$$\left[\frac{R_m(E_1)}{R_m(E_2)}\right] \Big/ \left[\frac{R_t(E_1)}{R_t(E_2)}\right] = K \qquad 3.4$$

was determined and compared with the theoretical value, E_2/E_1 . An additional determination of K was obtained from a comparison of the transitions to the ground state and first excited state in the reaction $^{149}Sm\ (n, \alpha)\ ^{146}Nd$ obtained directly by Beg and obtained with the electrostatic particle guide. The results are shown in Table 3.1 . The measured values of K are in reasonable agreement with the theoretical values, and for this reason, $K = E_2/E_1$ was used except for E_2/E_1 greater than 1.3.

3.4 Calculation of Penetrabilities and Reduced Widths

The barrier penetrability factors for an alpha particle were calculated using the method of Rasmussen [11]. In this technique the natural logarithm of the penetrability factor, P , is equal to twice the WKB integral

$$\ln(P) = -2 \int_{R_i}^{R_o} \frac{(2M)^{\frac{1}{2}}}{\hbar} \left[V(r) + \frac{2Ze^2}{r} + \frac{\hbar^2 L(L+1)}{2Mr^2} - E \right]^{\frac{1}{2}} dr \quad . \qquad 3.5$$

R_i and R_o are the inner and outer turning points respectively where the integrand vanishes. M is the reduced mass of the alpha particle, Ze is the charge of the daughter nucleus, L is the orbital angular momentum of the emitted alpha particle and E is the total alpha particle decay energy including recoil energy plus screening correction. V(r) is the nuclear potential and for the present calculations the Igo [29] potential was used. It is given by

$$V(r) = -1100 \exp\left[-\left(\frac{r - 1.17\, A^{1/3}}{0.574} \right) \right] \quad \text{MeV} \quad . \qquad 3.6$$

Table 3.1

Comparison of Experimental and Theoretical

Energy Correction Factor, K

K	E_2/E_1	Source
1.038 ± 0.034	1.051	$^{149}Sm(n,\alpha)^{146}Nd$
1.109 ± 0.044	1.109	^{226}Ra source
1.143 ± 0.037	1.174	
1.268 ± 0.042	1.302	
1.260 ± 0.052	1.313	
1.397 ± 0.056	1.455	
1.597 ± 0.055	1.709	

The integrations were carried out numerically using a program written for the IBM 7040 computer. The integrand was solved for R_i and R_o by an iterative procedure. Using these values the integral was then obtained by dividing the barrier region into 128 intervals and using a modified Simpson's rule.

From the measured thermal neutron (n, α) cross sections, $\hat{\sigma}_{n\alpha}$, the experimental alpha reduced widths, δ^2_{exp} , were determined from the formula

$$\delta^2_{exp} = 2\pi \Gamma_\gamma \frac{\hat{\sigma}_{n\alpha}}{\sigma_{n\gamma}} \frac{1}{\sum_L P_L} \quad . \qquad 3.7$$

This formula accounts for all possible L-waves in the alpha decay of the capture state. Γ_γ and $\sigma_{n\gamma}$ are the radiation width for gamma decay and the (n, γ) cross section respectively (where $\Gamma_\gamma \approx \Gamma_{total}$).

CHAPTER IV

SAMARIUM 149 RESULTS

The first experiments with the electrostatic particle guide technique were a study of the $^{149}Sm\ (n_{th}, \alpha)\ ^{146}Nd$ reaction. The major features of this reaction are well known from the studies of Macfarlane *et al* [1], Cheifetz *et al* [2], Beg [32] and others [21,33,34]. These studies yielded information on the more easily detectable transitions to the ground state and first excited state of ^{146}Nd. The present work has shown many fine structure peaks in the alpha particle spectrum corresponding to alpha decay to higher excited states of ^{146}Nd.

Neutron capture for ^{149}Sm in the thermal region is dominated by a resonance at 0.0967 eV [35] with a spin and parity 4^- [36,37,38] resulting from the $I+\frac{1}{2}$ addition of an s-wave neutron to the nuclear spin of ^{149}Sm, $I = 7/2^-$. The effective cross section of this resonance is $\sigma_{n\gamma}(4^-) = 64700$ barns [39]. In addition to this resonance there is a 1/v component [39] due to a bound 3^- level [1,2,32,33,34] with an effective cross section $\sigma_{n\gamma}(3^-) = 4800$ barns.

Alpha decay to the first excited state of ^{146}Nd is the most intense, and a factor of about seven higher than the transition to the ground state despite the Coulomb hindrance. This is explained by the strong 0.0967 eV 4^- resonance which can alpha decay to the 2^+ level in ^{146}Nd, but not to the ground state since parity conservation forbids a $4^- \rightarrow 0^+$ alpha decay transition. The transition to the ground state arises from the 3^- bound level of ^{150}Sm.

During the development of the electrostatic particle guide several studies were made of the $^{149}Sm\ (n, \alpha)\ ^{146}Nd$ reaction. The spectra of the two final measurements are shown in Figure 9 and Figure 10. The results presented in this chapter were obtained from these two experiments.

Figure 9 shows the spectrum obtained from a 1.4 mg target (35 $\mu g/cm^2$) of samarium enriched to 97.5% in ^{149}Sm. The spectrum, A , was obtained by irradiating the target for 235 hours in the thermal column of the McMaster reactor at a flux position of 10^{10} $n/cm^2/sec$. The particle guide was operated at 28 kV with a 0.05 cm diameter axial wire. The background spectrum, B , was obtained in 97 hours under the same conditions as spectrum A except that the target was reversed. Thus, the 1 mm thick aluminum target backing prevented alpha particles from the $^{149}Sm\ (n, \alpha)\ ^{146}Nd$ reaction from reaching the detector. Is is noted that the background increases as the particle energy decreases and that there are no peaks.

The second spectrum, which is shown in Figure 10, was obtained under similar conditions as before in 301 hours with a 2.2 mg target of ^{149}Sm (55 $\mu g/cm^2$). The notable exception was the installation of a bismuth plug in front of the particle guide to reduce the gamma field at the detector and reduce the background. This lower background is evident in that the spectrum no longer rises at low energies and several more transitions are evident at low energies.

The most intense peaks labelled A and B (right hand scale) correspond to alpha decay from the capture states of ^{150}Sm to the ground

Figure 9: ^{149}Sm Spectrum

A) Alpha particle spectrum from the $^{149}Sm\ (n, \alpha)^{146}Nd$ reaction; T = 235 hours.

B) Background spectrum with the sample backing only; T = 97 hours.

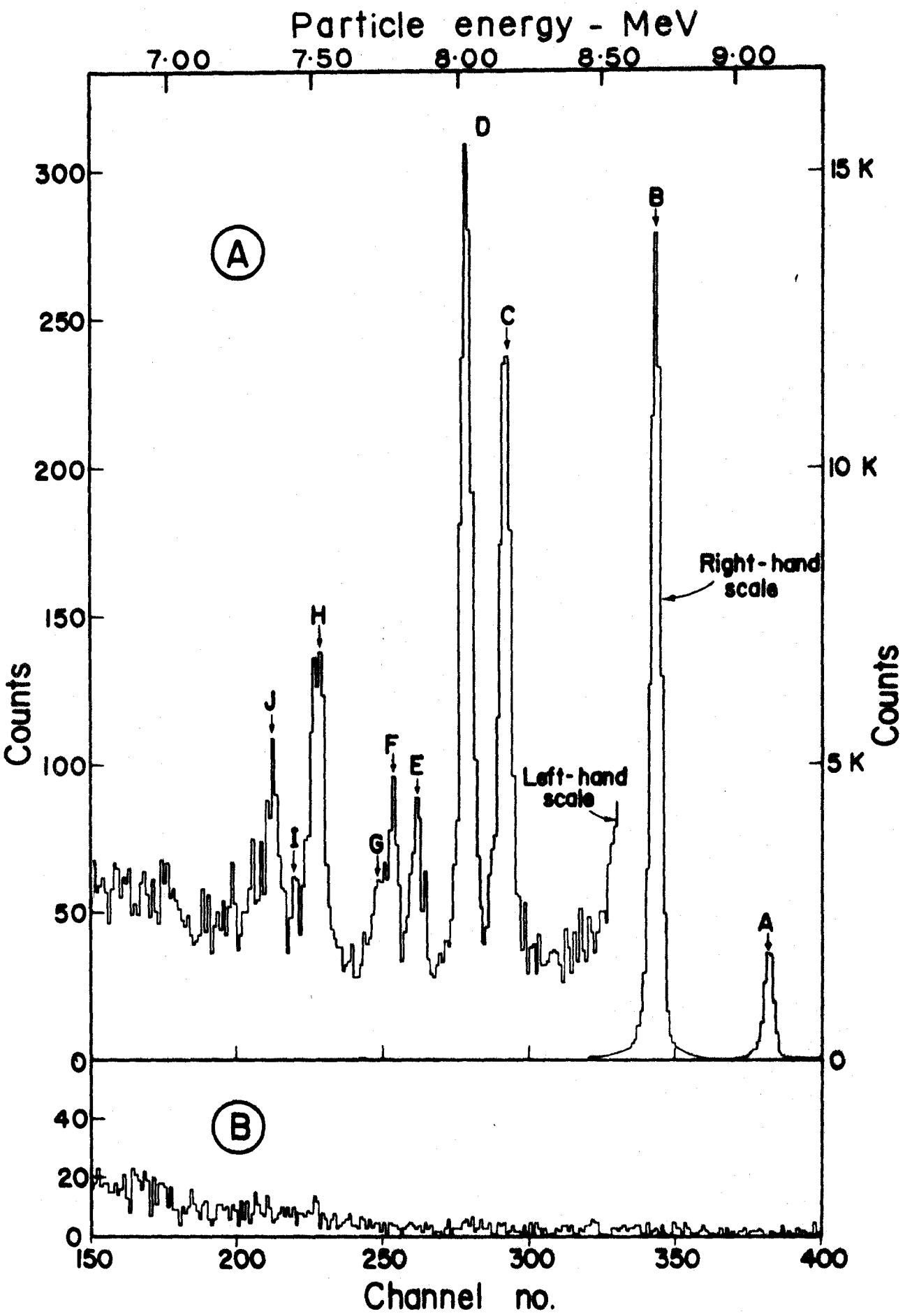
Particle energy - MeV
7·00
7·50
8·00
8·50
9·00
A
B
C
D
E
F
G
H
I
J
Right-hand scale
Left-hand scale
Counts
15 K
10 K
5 K
300
250
200
150
100
50
0
40
20
150
200
250
300
350
400
Channel no.

Figure 10: ^{149}Sm Spectrum

The alpha particle spectrum from the $^{149}Sm\ (n, \alpha)\ ^{146}Nd$ reaction is shown; T = 301 hours. The lower background was achieved by introducing a canned bismuth plug in front of the electrostatic particle guide to reduce the gamma flux at the detector.

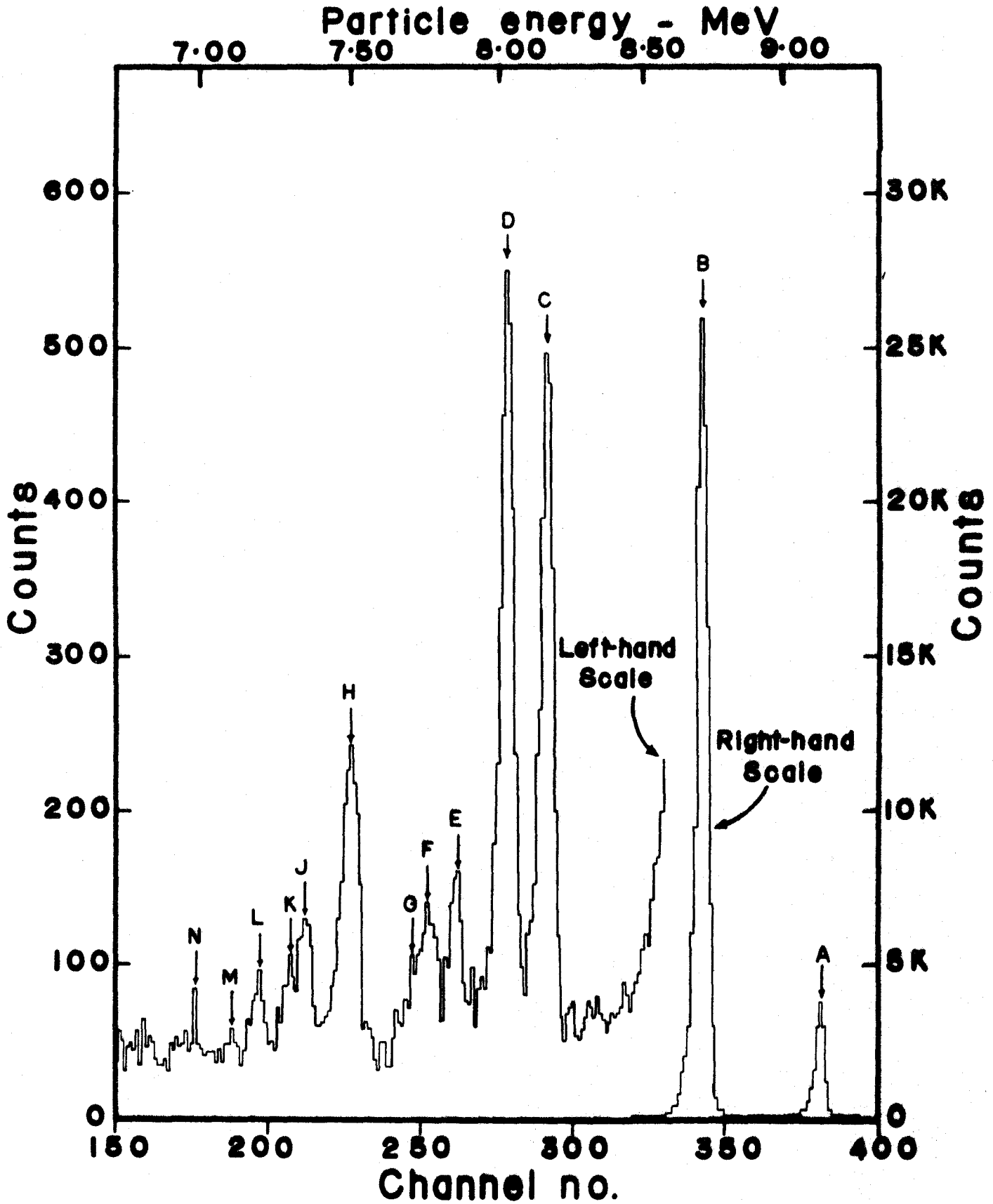
Particle energy - MeV
7·00
7·50
8·00
8·50
9·00
600
500
400
300
200
100
0
Counts
30K
25K
20K
15K
10K
5K
0
Counts
D
C
B
A
H
J
K
L
M
N
G
F
E
Left-hand Scale
Right-hand Scale
150
200
250
300
350
400
Channel no.

state and first excited state of ^{146}Nd respectively. Many of the other peaks labelled C through N correspond to known levels in ^{146}Nd. Peaks E through N were observed by Andreev [21] as a broad distribution. In the first spectrum, which has a resolution of 42 keV, there is evidence for a low intensity peak, I . This does not show up in the second spectrum because of the poorer resolution of 55 keV. An examination of the widths of the various peaks in the first spectrum where the resolution is better indicates that peak H may be a doublet separated by 10 to 20 keV. The doublet, F-G , is evident in both spectra. Because of the lower background, peaks K and L are more prominent in the second spectrum. As well, there is evidence for peaks at the positions labelled M and N.

Peak positions and alpha particle energies were determined by the methods outlined in Chapter III. For a well-separated peak, the mean of a Gaussian fit to the data by a non-linear least squares technique was adopted as the peak position. For doublets, such as peaks F-G and peaks J-K , the technique was modified by fitting to the experimental data the sum of two Gaussians, each with the same width. This five parameter fit gave the amplitudes, peak positions, and peak width for the two members of the doublet. Examples of these calculations are shown in Figures 11 and 12 which show the analysis of portions of the spectrum of Figure 10.

In Figure 11, a Gaussian was fit to peak E and its contribution subtracted from peaks F and G. This residual spectrum was then analyzed as above with the results indicated. The solid line represents the overall fit to the data and the dotted curves, the constituent Gaussians. A similar analysis of peaks J, K and L is shown in Figure 12. In both cases the excess of measured events over the fitted spectrum on the low energy

Figure 11: Peaks E, F and G

The portion of the alpha spectrum of Figure 10 containing peaks E, F, and G is shown on an expanded scale by a histogram. The continuous curve indicates the Gaussian fit to the data. The dotted portions indicate the constituent Gaussians from which the peak positions were determined.

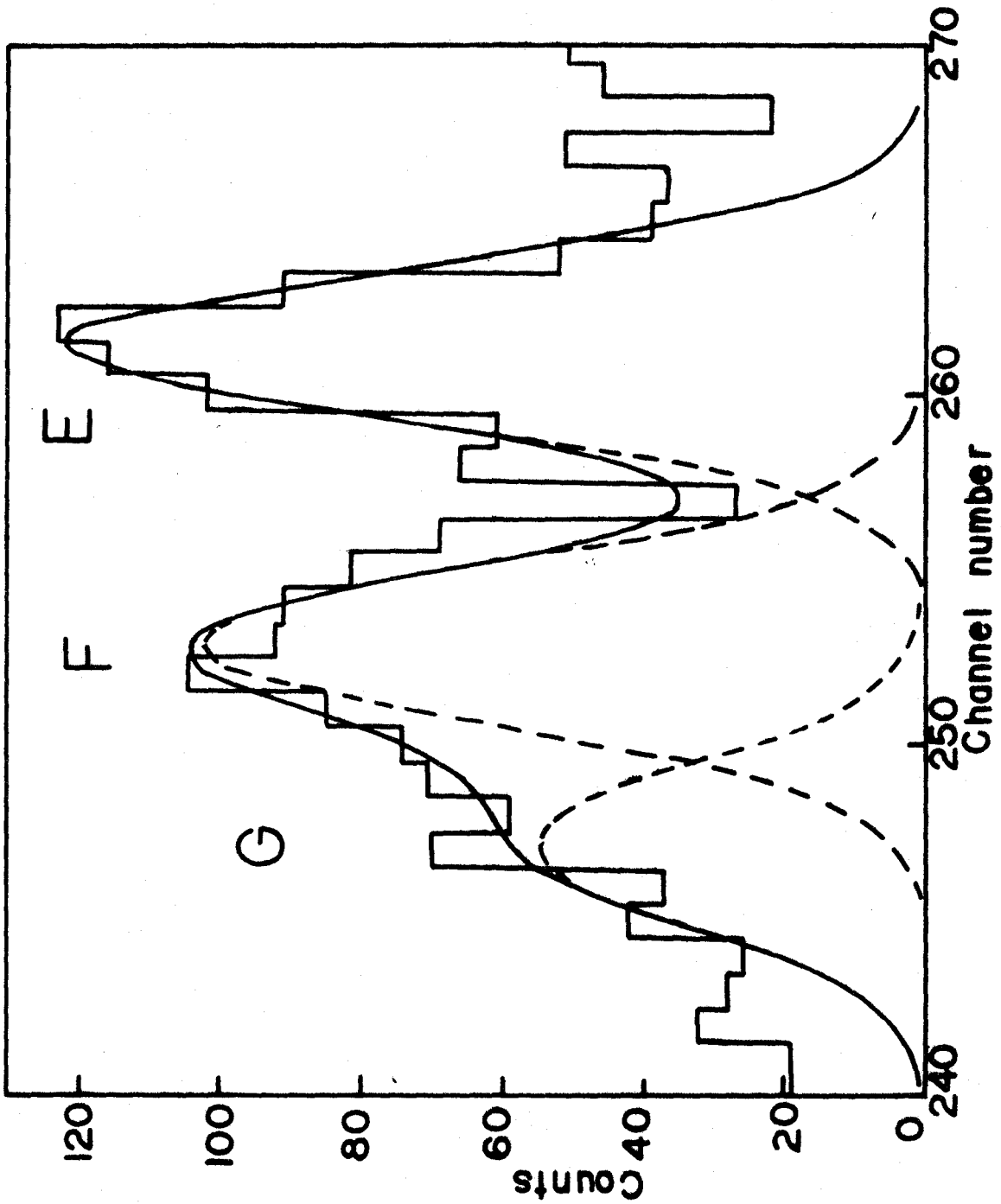
E
F
G
Counts
Channel number
0
20
40
60
80
100
120
240
250
260
270

Figure 12: Peaks J, K and L

The portion of the alpha particle spectrum of Figure 10 containing peaks J, K and L is shown on an expanded scale by a histogram. The continuous curve indicates the Gaussian fit to the data. The various Gaussians used to determine the peak positions are indicated by the dashed curves.

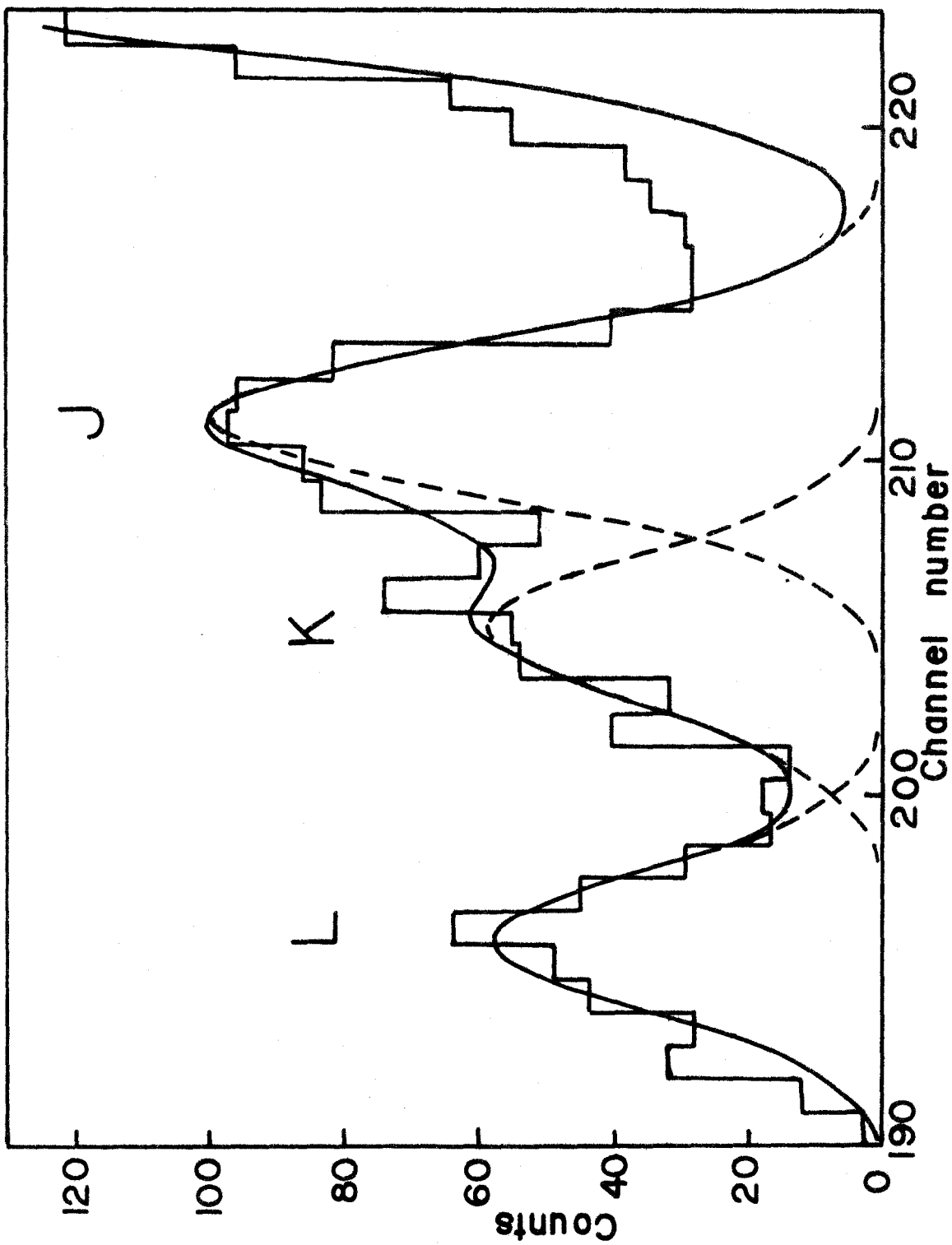
Counts
0
20
40
60
80
100
120
190
200
210
220
Channel number
J
K
L

side is from low energy tailing due to the thickness of the source and indicates the extent to which the measured spectrum differs from a true Gaussian shape.

The results of the analysis of both spectra were averaged to obtain the peak energies listed in Table 4.1 . The quoted errors in the energies are composed of ±3 keV in the 8.734 MeV peak which was used as a calibration point and the uncertainty in the peak positions. From the energies the corresponding excitation energies, E_x , were calculated from equations (3.1) and (3.2) and are also listed in Table 4.1 .

Relative cross sections were determined as outlined in Chapter III from the spectrum after correcting for the background and the low energy tail of the intense transitions to the ground state and first excited state. The effective thermal neutron (n, α) cross sections were then obtained by normalizing to peak B, the transition to the first excited state. Using the value of 38.7 mb for this transition [28] and averaging the results obtained from the two spectra, the values shown in Table 4.1 were obtained. The errors quoted contain the uncertainties in the cross section of the transition to the first excited state and in the areas of the peaks.

From the measured alpha energies, penetrabilities were calculated for each transition for the various contribuling L-values. Because there are two capture states in ^{150}Sm which contribute to the (n, α) cross section, equation (3.7) must be modified as follows to account for this.

$$\delta^2_{exp} = 2\pi \hat{\sigma}_{n\alpha}\left[\frac{\sigma_{n\gamma}(3^-)}{\Gamma_\gamma(3^-)}\sum_L P_L + \frac{\sigma_{n\gamma}(4^-)}{\Gamma_\gamma(4^-)}\sum_L P_L\right]^{-1} \qquad 4.1$$

Table 4.1

Summary of Results of Studies of the $^{149}Sm(n_{th}, \alpha)^{146}Nd$ Reaction

Peak	Energy	Cross Section	E_x	δ^2_{exp}	J^π
A	9.177 ± 0.003 MeV	5.29 ± 0.17 mb	0 keV	1.12 eV	0^+
B	8.734 ± 0.003	38.7 ± 1.2	455 ± 4	2.22	2^+
C	8.161 ± 0.004	669 ± 24 μb	1044 ± 5	0.15	(4^+)
D	8.018 ± 0.004	792 ± 28	1191 ± 5	0.52	3^-
E	7.835 ± 0.005	209 ± 13	1379 ± 6	0.58	
F	7.743 ± 0.005	175 ± 15	1474 ± 6	0.74	
G	7.683 ± 0.006	97 ± 9	1535 ± 7	0.56	
H	7.470 ± 0.005	377 ± 18	1754 ± 6	6.10	
I	7.39 ± 0.01	⩽37	1840 ± 10	⩽0.91	
J	7.313 ± 0.006	148 ± 11	1915 ± 7	5.48	
K	7.245 ± 0.006	88 ± 10	1985 ± 7	4.69	
L	7.148 ± 0.004	83 ± 10	2085 ± 5	7.64	
M	7.06 ± 0.02	⩽28	2180 ± 20	⩽4.3	
N	6.94 ± 0.02	⩽37	2300 ± 20	⩽11.2	

In the calculations it was assumed that $\Gamma_\gamma(3^-) = \Gamma_\gamma(4^-) = 0.058$ eV [39]. In the case of the first four levels, spins and parities are known and the reduced widths were calculated from equation (4.1) using the penetrabilities shown in Table 4.2 .

For most of the levels, however, the spins and parities are not known and an estimate of the reduced widths was made as follows. An examination of Table 4.2 shows that the alpha wave from the 4^- capture state with minimum L, L_{min}, contributes about 2/3 of the total (n, α) cross section. Thus the reduced width can be estimated from

$$\delta^2_{exp} = \frac{2}{3} \frac{2\pi \hat{\sigma}_{n\alpha} \Gamma_\gamma(4^-)}{\sigma_{n\gamma}(4^-) P_{L_{min}}} \qquad 4.2$$

where $L_{min} = (4 - J)$ or $(4 - J) + 1$ to conserve parity, where J is the spin of the level in ^{146}Nd. The values of L_{min} for various possible J^π for peak E are listed in Table 4.2 along with the penetrabilities and reduced widths calculated from equation (4.2). The reduced widths for the other peaks calculated for the same choices of L_{min} are in the same ratio as those for peak E. For this reason only the values of δ^2_{exp} for $L_{min} = 3$ are presented in Table 4.1 which summarizes the results.

Figure 13 shows the level scheme of ^{146}Nd obtained by studying the alpha decay of the capture states of ^{150}Sm. Excitation energies in MeV are shown at the left. The intensity of each transition as a percentage of the total (n, α) cross section is indicated by the numbers in the brackets above each level. Alpha decay of the capture state represents only $6.75 \times 10^{-5}\%$ of the total decay probability with gamma decay accounting for greater than 99% .

Table 4.2

Calculation of Reduced Widths

Peak	Energy	J^π	L-value	P_L	δ^2_{exp}
A	9.177 MeV	0^+	3	3.597×10^{-7}	1.12
B	8.734	2^+	1	1.722×10^{-7}	2.22
			3	0.671	
			5	0.126	
C	8.161	(4^+)	1	15.97×10^{-9}	0.15
			3	6.08	
			5	1.09	
			7	0.09	
D	8.018	3^-	0	10.22×10^{-9}	0.52
			2	5.69	
			4	1.47	
			6	0.18	
			L_{min}		
E	7.834	$[3^+,4^+,5^+]$	1	3.63×10^{-9}	0.22
		$[2^-,3^-,5^-,6^-]$	2	2.45	0.32
		$[1^+,2^+,6^+,7^+]$	3	1.36	0.58
		$[1^-,7^-,8^-]$	4	0.63	1.26

Figure 13: ^{146}Nd Decay Scheme

The alpha decay scheme of the thermal neutron capture states of ^{150}Sm is shown. The excitation energies of the levels of ^{146}Nd are shown at the left. The percentage of the total (n,α) cross section to each level is indicated by the number in brackets.

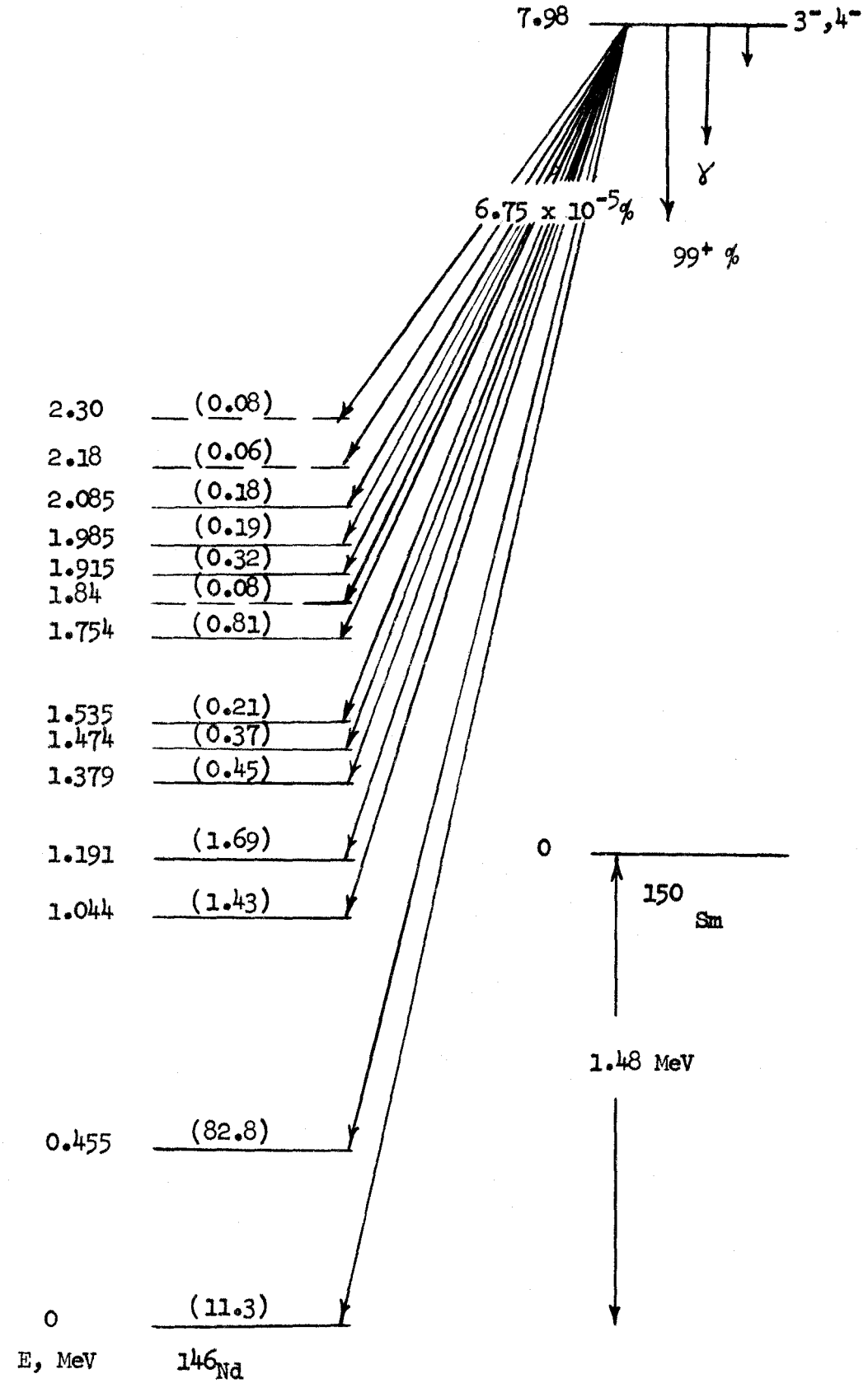

Many of the levels found in the (n,α) studies correspond to levels known from the electron capture studies of ^{146}Pm (30) and from beta decay studies of ^{146}Pr (31). These results are compared in Table 4.3. The agreement in the energies is very good with the exception of the peak (H) at 1754 keV which is reported as 1720 keV (31). Daniels *et al* (40), however, reported 1750 keV for this level. In the present (n,α) study there is no evidence for the reported level at 1233 keV and new levels are found at 1474, 1535, 1915, and 2085 keV with possible levels at 1840 and 2300 keV.

A detailed discussion of the reduced widths will be left until Chapter VII after the results of the studies of ^{143}Nd and ^{147}Sm have been presented. An examination of Table 4.1 shows that there are some-fluctuations in the reduced widths for the alpha transitions to levels up to about 1.6 MeV. Above this energy there are several transitions which appear to be enhanced.

Table 4.3

Level Scheme of ^{146}Nd Obtained from the $^{149}Sm(n_{th}, \alpha)^{146}Nd$ Reaction Compared with Results of β, γ Studies

Energy Levels - keV		
Present Work	Reference (10)	Reference (11)
0	0	0
455 ± 4	453.9 ± 0.3	455 ± 5
1044 ± 5	1043 ± 1	1050±10
1191 ± 5	1190.2 ± 0.6	1200± 15
	(1233)*	
1379 ± 6		1370±20
1474 ± 6		
1535 ± 7		
1754 ± 6		1720±20
(1840±10)*		
1915 ± 7		
1985 ± 7		1970±30
2085 ± 5		
(2180±20)*		2220±20
(2300±20)*		
		2720±20

*uncertain because of low intensity

CHAPTER V

NEODYMIUM 143 RESULTS

The study of the $^{143}Nd\ (n, \alpha)\ ^{140}Ce$ reaction has in many ways proven to be the most rewarding. Only the most intense transition to the ground state of ^{140}Ce had been measured in previous studies [2,21,28] because of the high energy of the first excited state at 1.6 MeV and its consequently much smaller cross section. Only upper limits could be set by these studies on the transitions to this and higher levels. In the present study, utilizing the high peak to background ratio of the electrostatic particle guide, alpha transitions to at least eight levels in ^{140}Ce have been detected. In addition, there is evidence for a process involving a gamma decay from the capture state of ^{144}Nd to lower lying states followed by alpha decay to the ground state of ^{140}Ce. Because theoretical studies have been made of ^{140}Ce [41], it has been easier to interpret the results of this chapter than the results of the $^{149}Sm\ (n, \alpha)\ ^{146}Nd$ reaction.

The only level in ^{144}Nd populated by thermal neutron capture is a bound level at - 6 eV with an effective neutron capture cross section of 335 ± 20 barns [42]. The ground state spin of ^{143}Nd is $7/2^-$ and thus s-wave neutron capture will yield 3^- or 4^- states. Since there is alpha decay to the ground state of ^{140}Ce, the capture state is 3^- since parity conservation forbids a $4^- \rightarrow 0^+$ alpha decay.

Figure 14 shows the alpha particle spectrum obtained from a 2.4 mg

Figure 14: ^{143}Nd Spectrum

The alpha particle spectrum for the $^{143}Nd\ (n, \alpha)\ ^{140}Ce$ reaction is shown; T = 580 hours. The scale for the ground state peak is on the right while the scale for the rest of the spectrum is on the left. The $(n,\gamma\alpha)$ reaction is also indicated.

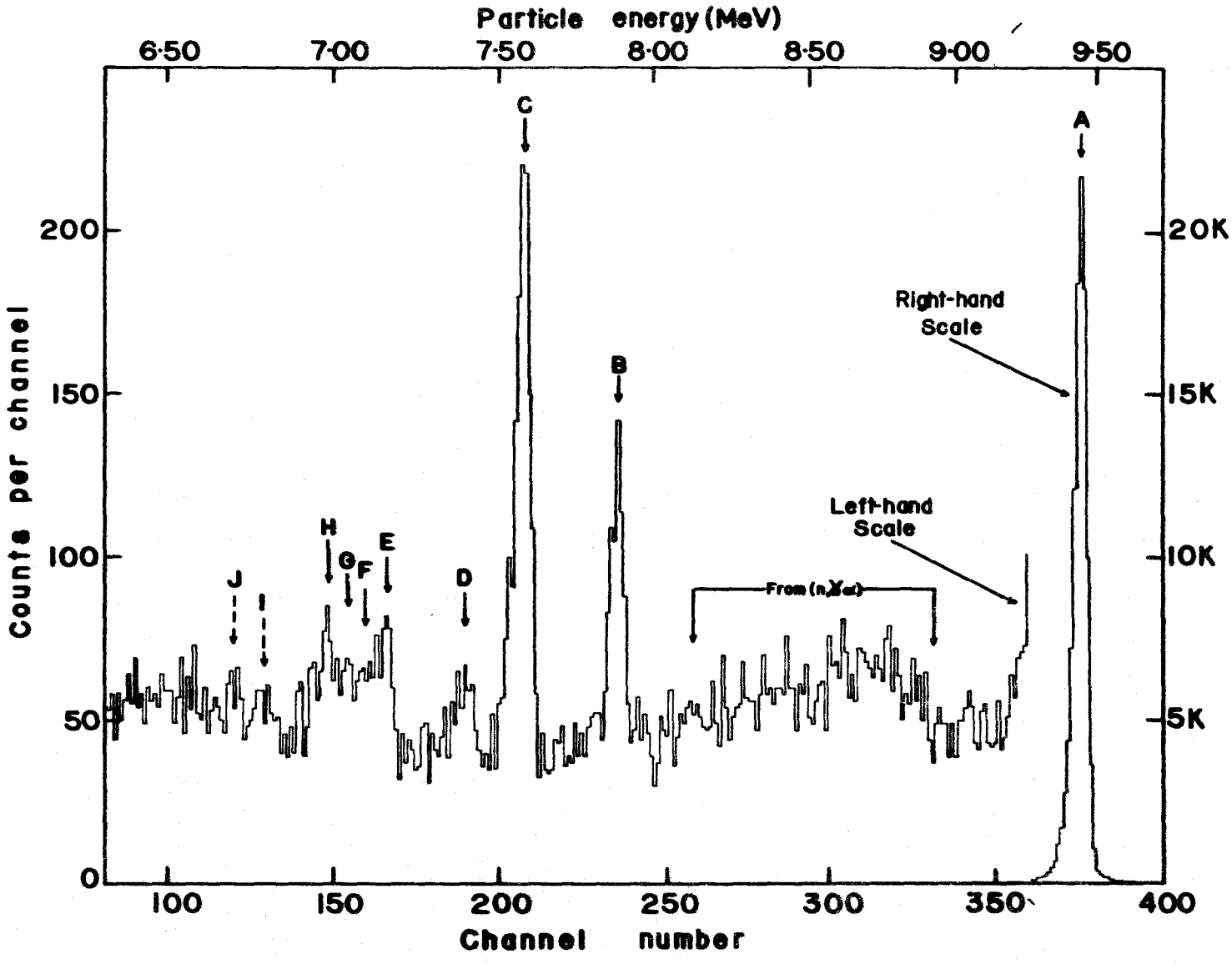
Particle energy (MeV)
6·50
7·00
7·50
8·00
8·50
9·00
9·50
Counts per channel
200
150
100
50
0
20K
15K
10K
5K
Right-hand Scale
Left-hand Scale
A
B
C
D
E
F
G
H
J
From (n,Xα)
100
150
200
250
300
350
400
Channel number

target of neodymium oxide enriched to 91.3% in ^{143}Nd (65 $\mu g/cm^2$). The spectrum was obtained in 580 hours at a flux position of 10^{10} $n/cm^2/sec$ as described previously. The particle guide was operated at 30 kV with a 0.6 cm diameter axial electrode.

The most intense peak (right hand scale) corresponds to alpha decay to the ground state of ^{140}Ce. Most of the other peaks, labelled B to J, correspond to known levels in ^{140}Ce [43] while peak G (as well as I and J) is unreported. Also evident is a broad distribution between the peaks labelled A and B which we believe is due to the $(n,\gamma\alpha)$ reaction.

Peak positions were obtained as before. In the case of peaks E, F, G, and H the spectrum was analyzed as follows. The portion of the spectrum containing these peaks is shown in Figure 15 with the background subtracted. It was analyzed by fitting a Gaussian to E and H and subtracting these peaks from the spectrum. Peaks F and G were obtained by fitting to the residual the sum of two Gaussians with the same width to obtain the results indicated in Figure 15. The solid curve represents the sum of the four peaks while the dotted portions indicate the individual Gaussians.

The energies of the various transitions calculated from the peak positions are presented in Table 5.1. The errors include the uncertainty in the peak positions and the uncertainty of ±3 keV in the energy of the 9.443 MeV peak (A) which was used as a normalization point [28]. The excitation energies calculated from equations (3.1) and (3.2) are also listed.

The relative cross sections were determined as outlined previously

Figure 15: Peaks E, F, G, and H

The portion of the alpha spectrum containing peaks E, F, G, and H is shown on an expanded scale by a histogram. The continuous curve indicates the Gaussian fit to the data. The dotted portions indicate the constituent Gaussians from which the peak positions were determined.

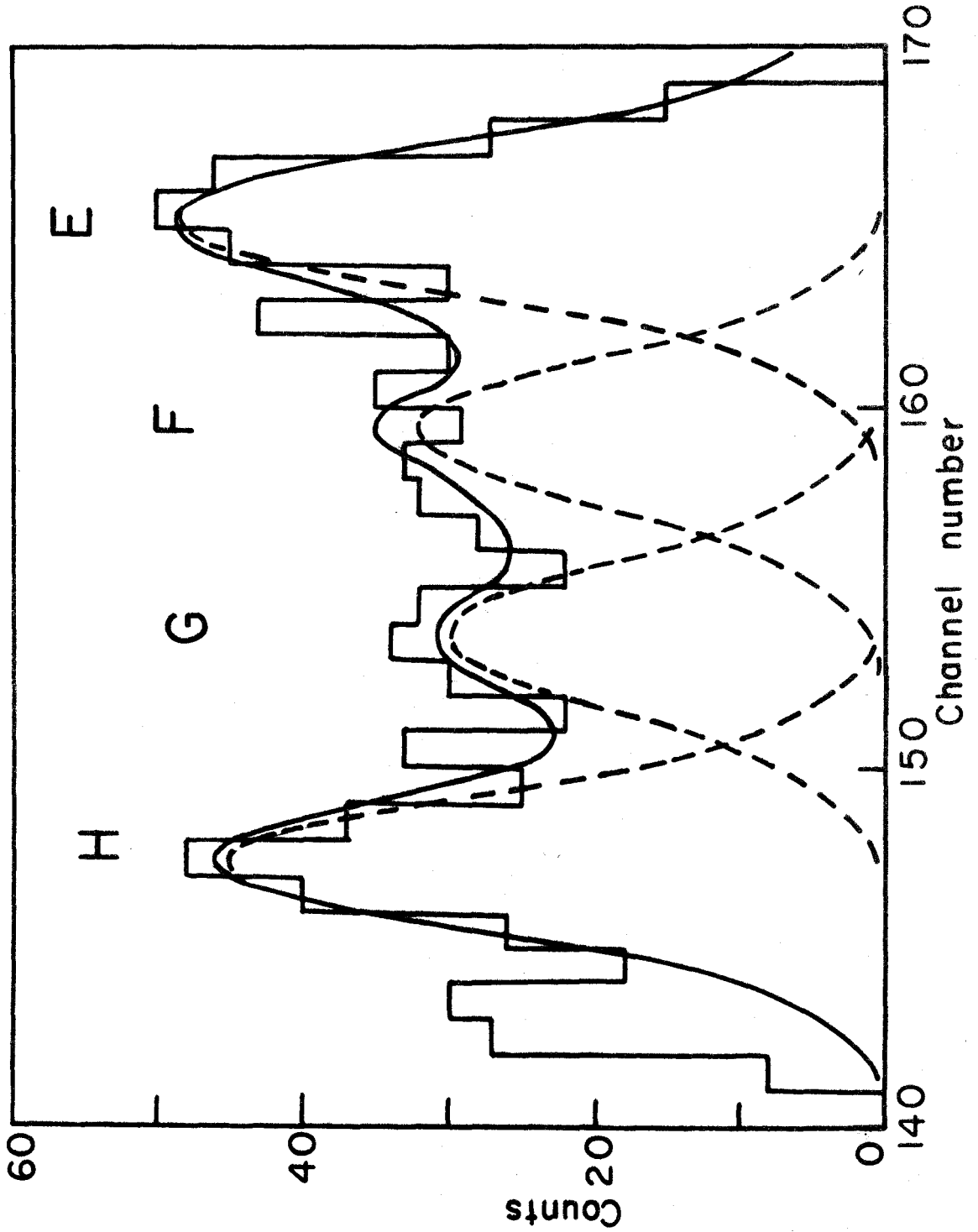
E
F
G
H
60
40
20
0
Counts
140
150
160
170
Channel number

Table 5.1

Summary of the Results of the $^{143}Nd(n,\alpha)^{140}Ce$ Reaction

Peak	Energy	Cross Section	E_x	J^π	L-value	P_L	δ^2_{exp}	E_x, Ref.(43)
A	9.443 ± 0.003 MeV	21.3 ± 0.64 mb	0 keV	0^+	3	2.78 x10^{-6}	12.4eV	0 keV
B	7.889 ± 0.005	83 ± 5 μb	1599 ± 6	2^+	1 3 5	1.86 x10^{-8} 0.69 0.12	5.0	1596.6 ± 0.3
C	7.591 ± 0.005	164 ± 7	1905 ± 6	0^+	3	1.70 x10^{-9}	156	1903.5 ± 0.3
D	7.410 ± 0.008	34 ± 3	2091 ± 9	4^+	1 3 5 7	2.00 x10^{-9} 0.73 0.12 0.01	19	2083.6 ± 0.3
E	7.165 ± 0.010	42 ± 3	2343 ± 10	2^+	1 3 5	5.45 x10^{-10} 1.96 0.32	88	2348.4 ± 0.3
F	7.107 ± 0.010	23 ± 3	2403 ± 10	3^+	1 3 5	4.05 x10^{-10} 1.46 0.24	65	2412.4 ± 0.3
G	7.051 ± 0.010	26 ± 3	2460 ± 10		1 3 5	3.00 x10^{-10} 1.08 0.17	99	
H	6.985 ± 0.010	36 ± 3	2528 ± 10	$(1^+,4^+)$	1 3 5	2.09 x10^{-10} 0.75 0.12	196	2516.1 ± 0.5 (4^+) 2521.8 ± 0.4 (1^+) 2547.5 ± 0.8
I	6.80 ± 0.02	≤14	2720 ± 20		2	4.84 x10^{-11}	≤470	
J	6.71 ± 0.02	≤12	2810 ± 20		2	2.89 x10^{-11}	≤670	

after correcting the spectrum for background and tailing from the large peak, A . The effective thermal neutron (n, α) cross sections were determined by normalizing the relative cross sections to peak A. Using a value of 21.3 ± 0.64 mb for this transition, the results shown in Table 5.1 were obtained. The errors quoted include the uncertainties in the areas of the peaks and the cross section of the ground state transition.

Reduced widths were calculated from the measured alpha particle energies and cross sections. Unlike ^{146}Nd, the spins and parities of most of the levels of ^{140}Ce are known. Using the method of Chapter III penetrabilities were calculated for each transition for each contributing L-value. These values of P_L are listed in Table 5.1 . The corresponding reduced widths were calculated from equation (3.7) using $\Gamma_\gamma(3^-) = 0.086$ eV and $\sigma_{n\gamma} = 335$ barns [42]. In the case of peak G for which J^π is not known, and for peak H which corresponds to a triplet, δ^2_{exp} was estimated by considering the contributions of $L = 1, 3$ and 5 . For the possible transitions J and I, an upper limit was placed on δ^2_{exp} by considering an $L = 2$ alpha wave as the major contribution.

The alpha decay scheme of the capture states of ^{144}Nd is shown in Figure 16 . Excitation energies and spins and parities of the levels are shown on the left. Intensities as a percentage of the total (n, α) cross section are also indicated. The ratio of the alpha decay probability to gamma decay probability is $5.2 \times 10^{-3}\%$ which is higher by two orders of magnitude than for the $^{149}Sm\ (n, \alpha)\ ^{146}Nd$ reaction. The total $(n,\gamma\alpha)$ intensity is estimated to be $\leqslant 2\%$ of the intensity of the alpha decay from the capture state to the ground state.

Figure 16: ^{140}Ce Decay Scheme

The alpha decay scheme of the thermal neutron capture states of ^{144}Nd is shown. The excitation energies and J^{π} of the levels of ^{140}Ce are shown at the left. The broad distribution due to the $(n,\gamma\alpha)$ reaction to the ground state of ^{140}Ce is also indicated.

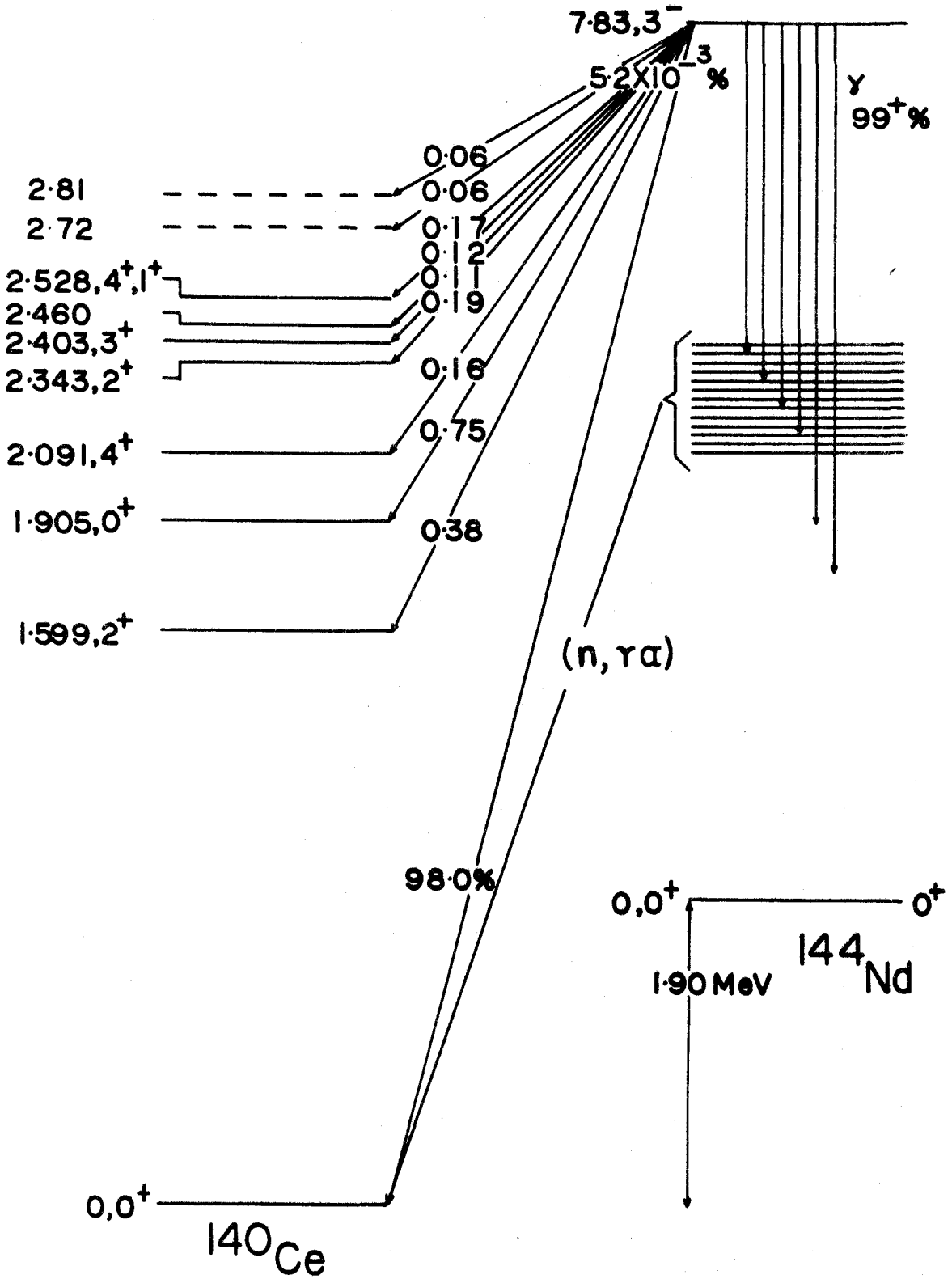
7·83,3⁻
5·2X10⁻³ %
γ
99⁺%
0·06
0·06
0·17
0·12
0·11
0·19
0·16
0·75
0·38
2·81
2·72
2·528,4⁺,1⁺
2·460
2·403,3⁺
2·343,2⁺
2·091,4⁺
1·905,0⁺
1·599,2⁺
(n,γα)
98·0%
0,0⁺
140Ce
0,0⁺
0⁺
1·90 MeV
144Nd

The excitation energies of many levels of ^{140}Ce are accurately known from the gamma decay studies of ^{140}Ce following the beta decay of ^{140}La (43) and these energies are shown in the table. The energies obtained from alpha decay studies are in good agreement with these, although the energy resolution in gamma decay studies using Li-Ge detectors is superior. The level at 2528 keV (H) obtained from alpha decay is seen to correspond to three close levels. The level at 2460 keV is unreported, as are the possible levels at 2720 and 2810 keV (peaks I and J).

The alpha reduced widths from the capture states of ^{144}Nd are found to be an order of magnitude higher than in the case of ^{150}Sm. This may be understood in terms of the statistical model and the effect of the 82 neutron closed shell which makes the level spacing for ^{144}Nd an order of magnitude larger than for ^{150}Sm. It is also evident that the transitions to several of the excited states of ^{140}Ce are enhanced by an order of magnitude. A discussion of this is deferred to Chapter VII.

CHAPTER VI

SAMARIUM 147 RESULTS

The $^{147}Sm\ (n,\alpha)\ ^{144}Nd$ reaction was studied last and the results of this experiment are presented here. In studies of this reaction by Cheifetz et al [2], decay of the capture states of ^{148}Sm was observed to the ground state and first excited state of ^{144}Nd. The results of the present experiment show these transitions as well as those to two higher excited states.

The thermal neutron capture states of ^{148}Sm are not well known. Since the ground state of ^{147}Sm has $J^{\pi} = 7/2^-$, the capture of an s-wave neutron will populate only 3^- or 4^- states. The appearance of the transition to the ground state of ^{144}Nd following thermal neutron capture indicates that at least one of the capture states of ^{148}Sm has $J^{\pi} = 3^-$. From the work of Poortmans et al [47] such a level is known at 3.4 eV. A level at 18.3 eV has $J^{\pi} = 4^-$. Cheifetz et al [2], however, assign 4^- to the level at 3.4 eV and 3^- to the levels at 18.3 eV and 27.1 eV to explain the higher alpha decay rate of the capture states of ^{150}Sm to the first excited state of ^{144}Nd (as compared to the ground state) without invoking the existence of a bound level as in the case of ^{149}Sm. The thermal neutron capture cross section of ^{147}Sm is 75 ± 11 barns (measured with $400^{\circ}K$ neutrons) [48].

Figure 17 shows the alpha particle spectrum obtained from a 5.5 mg target of samarium enriched to 97.8% in ^{147}Sm (140 $\mu g/cm^2$). The spectrum was obtained in 845 hours at a flux position of 10^{10} $n/cm^2/sec$.

Figure 17: ^{147}Sm Spectrum

The alpha particle spectrum of the $^{147}Sm\ (n, \alpha)\ ^{144}Nd$ reaction is shown: T = 845 hours.

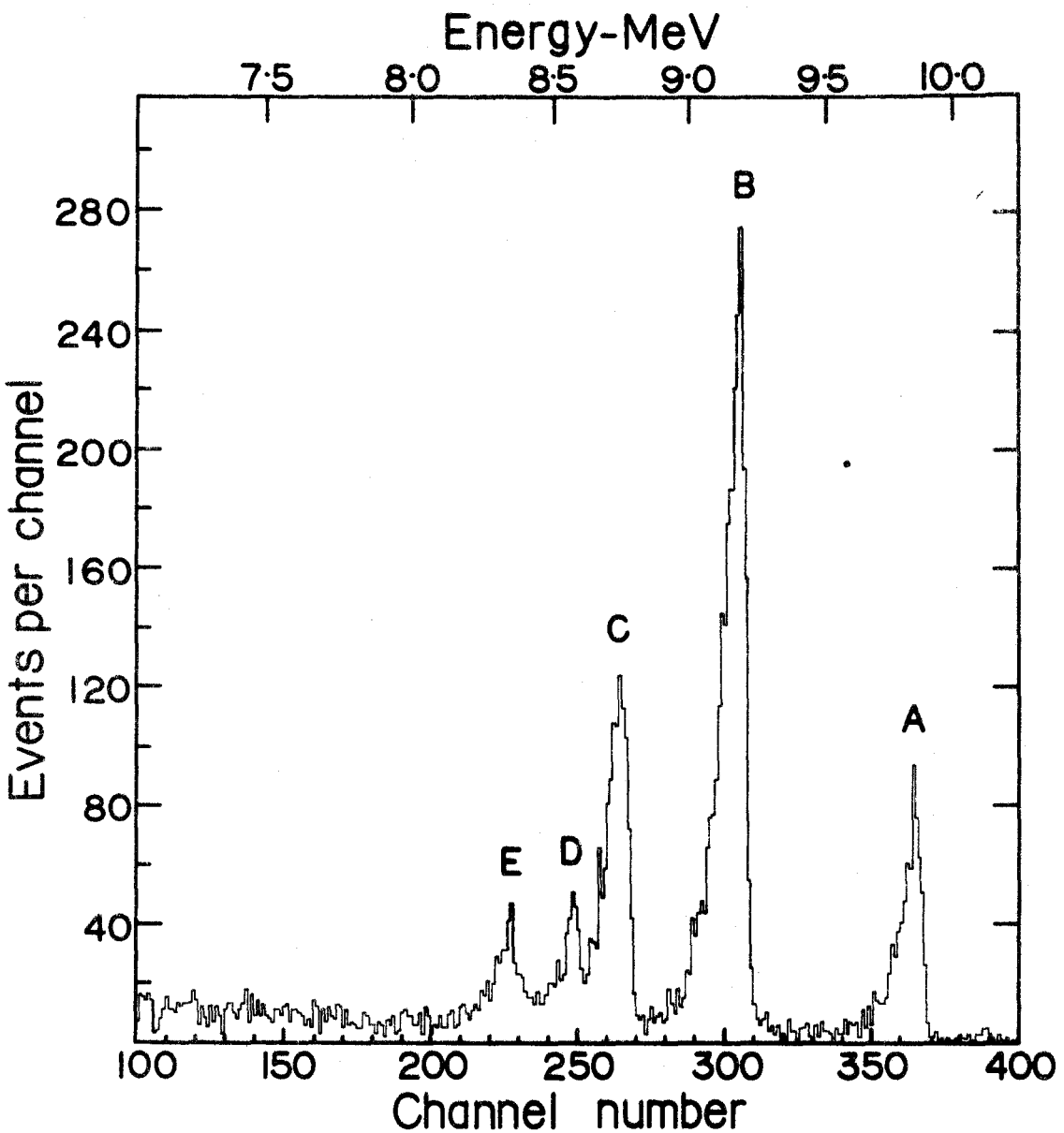
Energy-MeV
7·5
8·0
8·5
9·0
9·5
10·0
280
240
200
160
120
80
40
Events per channel
B
C
A
E
D
100
150
200
250
300
350
400
Channel number

The particle guide was operated at 30 kV with a 0.6 cm axial electrode.

The peaks labelled A, B, D, and E are due to ^{147}Sm, while the peak labelled C arises from an impurity of ^{149}Sm and is due to the alpha transition to the first excited state of ^{146}Nd. There is also a contribution to peak B from ^{149}Sm due to the transition to the ground state of ^{146}Nd. It is interesting that no peaks were seen at lower energies and in particular near channel 205 (8.10 MeV) which corresponds to a known level in ^{144}Nd.

Alpha energies were obtained as before by finding the peak positions and using peak C as a normalization point. The alpha energies are shown in Table 6.1 as well as the corresponding excitation energies. The errors quoted contain the uncertainties in the peak positions as well as the uncertainty in the energy of peak C, 8.734 ± 0.003 MeV [28].

Relative cross sections were obtained as before after correcting for background. Because of the thicker target, the spectrum exhibits considerable low energy tailing. This tail was subtracted from lower energy peaks by estimating the peak shape from the well separated peak, A. The effective thermal neutron cross sections were obtained by normalizing to the known cross section for the transition corresponding to peak C (38.7 ± 1.2 mb) and the known abundances of ^{147}Sm and ^{149}Sm in the target ($^{147}Sm = 97.8 \pm 0.1\%$, $^{149}Sm = 0.51 \pm 0.05\%$). These cross sections are listed in Table 6.1. The errors quoted include the uncertainties in the peak areas (including the background uncertainty), the cross section of the standard, and the isotopic abundances.

Reduced widths were calculated as before using equation (3.7) and

Table 6.1

Summary of the Results of the $^{147}Sm\ (n,\alpha)\ ^{144}Nd$ Reaction

Peak	Energy	Cross Section	E_x	J	L-value	P_L	σ^2_{exp}	E_x, Previous
A	9.844 ± 0.006 MeV	142 ± 17 μb	0 keV	0	3	3.15×10^{-6}	0.19 eV	0 keV
B	9.173 ± 0.006	395 ± 44	690 ± 8	2	1	8.00×10^{-7}	1.38	696.7 ± 0.6 (44)
					3	3.16		
					5	0.61		
D	8.562 ± 0.006	49 ± 8	1318 ± 8	4	1	7.96×10^{-8}	1.73	1313 ± 1 (45)
					3	3.07		
					5	0.56		
					7	0.05		
E	8.333 ± 0.10	48 ± 8	1553 ± 12	3	1	2.94×10^{-8}	4.63	1520 (46)
					3	1.12		1556 ± 8 (45)
					5	0.20		

$\Gamma_\gamma(3^-) = 0.049$ eV [49] and $\sigma_{n\gamma} = 75$ barns [48]. The contributing L-values and corresponding penetrabilities are shown in Table 6.1 along with the values of δ^2_{exp}.

The alpha decay scheme of Figure 18 shows four levels in ^{144}Nd populated by alpha decay of the capture states of ^{148}Sm. The excitation energies and intensities are indicated.

As shown in Table 6.1, the excitation energies obtained here are in good agreement with those from (n,γ) studies with ^{143}Nd [45] and beta decay studies of ^{144}Pr [44]. There are two reported levels at 1520 and 1556 keV which bracket the measured energy of peak E of 1553 keV. An examination of peak E reveals a high energy tail which is not present in the other peaks and could be due to the reported doublet.

With the exception of the ground state, the reduced widths show little fluctuation, especially if peak E is a doublet. The reduced widths are very close to those obtained for the alpha decay of the capture states of ^{150}Sm. The fact that the ground state transition has a reduced width so much smaller than the transition to the first excited state is suspicious. It is possible that the decay of ^{148}Sm to the ground state of ^{144}Nd is due to the 3^- capture state at 3.4 eV and that there is an additional 4^- bound level which contributes to the cross section for the alpha decay to the excited states of ^{144}Nd.

Figure 18: ^{144}Nd Decay Scheme

The alpha particle decay scheme of the thermal neutron capture states of ^{148}Sm is shown. The excitation energies of the levels of ^{144}Nd are shown at the left. The measured intensities are indicated as a percentage of the total (n,α) cross section.

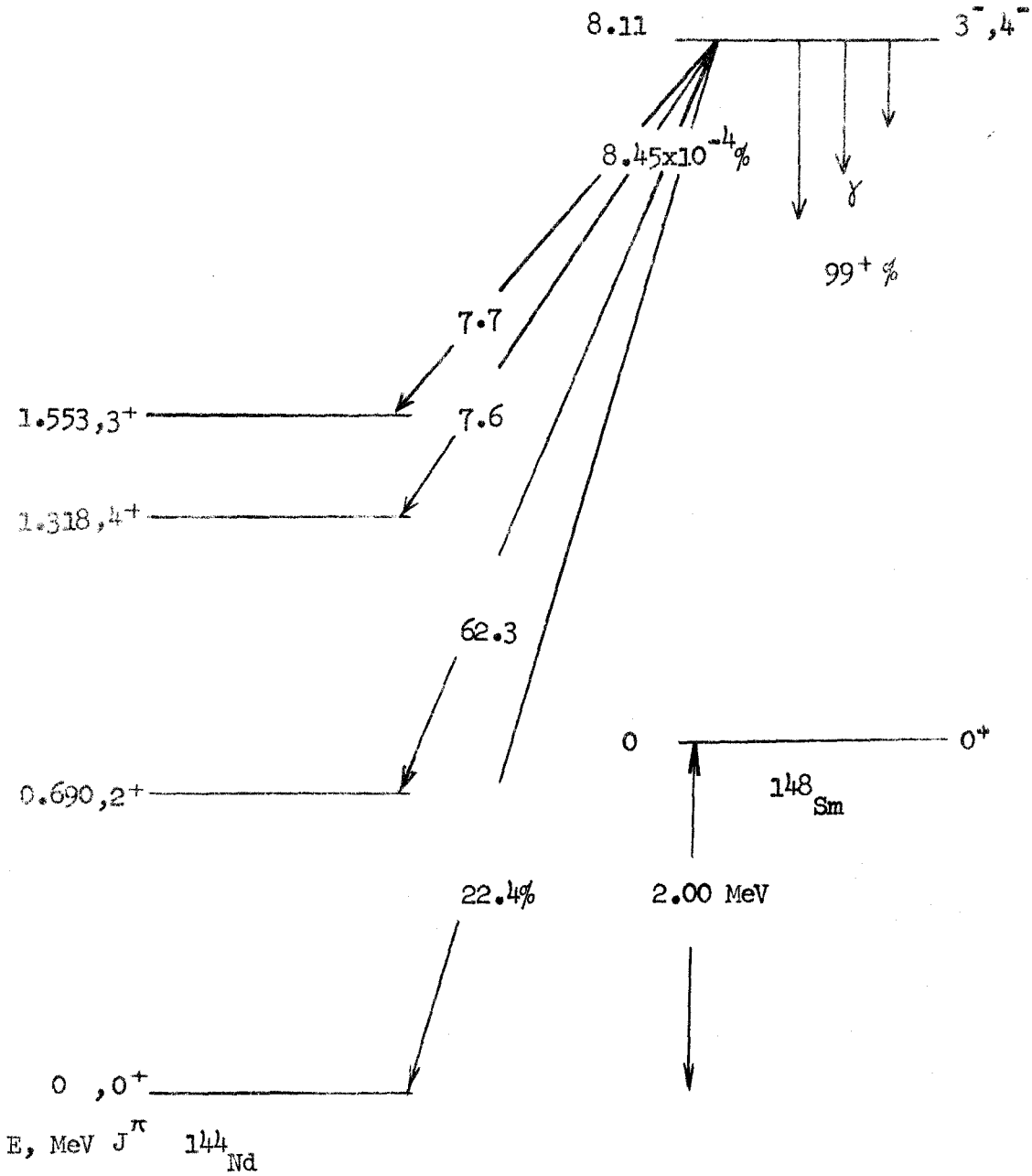
8.11
3⁻,4⁻
8.45x10⁻⁴%
γ
99⁺ %
7.7
7.6
1.553,3⁺
1.318,4⁺
62.3
0
0⁺
148Sm
0.690,2⁺
22.4%
2.00 MeV
0 ,0⁺
E, MeV Jπ 144Nd

CHAPTER VII

DISCUSSION OF RESULTS

7.1 General

This discussion of the (n, α) reaction will include a description of the information which can be obtained by this type of study, the limitations of the technique, and suggestions about future investigations that can be made using this method of studying the nucleus. The types of information that can be obtained are as follows.

Although little emphasis has been placed on the measurement of ground state Q-values in this study, these are important. They provide an independent measurement which can be compared with values obtained from mass data.

It has been seen from the results of the previous three chapters that level schemes can be obtained for the daughter nucleus. The results obtained from alpha decay studies are in good agreement with information from other sources. Alpha decay has no strong angular momentum selection rule (except that parity must be conserved). Because of this it was possible to detect all levels up to about 2.5 MeV excitation and as well, several new levels were found. It must be admitted, however, that the resolution in alpha decay studies is certainly worse than in gamma decay studies with Li-Ge detectors.

It is possible in certain cases to investigate the spin and parity of the capture state by means of the (n,α) reaction. In the case of odd neutron targets, the ground state of the daughter nucleus is 0^+. Knowing the spin and parity of the target nucleus there are two possible spins

for the compound system for s-wave neutron capture. One can decide which one is populated by determining if alpha decay to the 0^+ ground state occurs.

The alpha reduced widths contain all the information dependent on nuclear properties in the alpha decay process. The study of the nature of levels in a region of high level density, and in particular thermal neutron capture states, is facilitated by an investigation of the fine structure in the decay of the capture states and the corresponding reduced widths. A discussion of the reduced widths is given in the last section of this chapter.

There is also evidence for alpha decay from levels below the neutron separation energy in the $^{143}Nd\ (n,\alpha)\ ^{140}Ce$ reaction study. This process, the $(n,\gamma\alpha)$ reaction, is discussed in detail in the next section.

There are certain limitations in the (n,α) reaction studies which must be considered. The alpha transition probability is very sensitively dependent on alpha energy. Because of this, one is limited to studying transitions to levels up to a few MeV excitation. Even for reasonable source thicknesses of 30 to 50 $\mu g/cm^2$ the low energy tail from intense transitions to the ground state or low lying excited states is a problem. In the region above 2 to 3 MeV excitation this tail and the fact that the level spacing is decreasing makes it difficult to resolve individual peaks.

The Coulomb hindrance also limits the possible nuclei which one can study. In the rare earth region several nuclides have a Q-value of 8 to 10 MeV for alpha decay from the capture state to the ground state. This is still well below the Coulomb barrier height. However, the

possibility of observing the weak alpha decay branch in competition with the predominant gamma decay mode is enhanced by studying nuclei with a large neutron capture cross section. Thus one is restricted to using targets which have a high Q-value and a large capture cross section - usually odd neutron isotopes.

Future investigations of (n,α) reactions should include a study in a region of deformed nuclei. Targets of ^{155}Gd and ^{157}Gd are a good choice for studying alpha decay from neutron capture states to a rotational band in the daughter.

By modifying the existing technique to use a higher neutron flux and by using a detector which covers the whole end area of the electrostatic particle guide the count rate could be increased significantly. It should then be possible to study systematically the (n,α) reaction for many nuclei throughout the periodic table.

7.2 The $(n,\gamma\alpha)$ Reaction

The spectrum of the reaction $^{143}Nd\ (n,\alpha)\ ^{140}Ce$ shown in Figure 14 reveals a broad distribution of alphas between the ground state and first excited state transitions. These alphas are believed to come from the reaction whereby the capture state of ^{144}Nd emits a gamma ray and deexcites to a level below the capture state. This state then, has a probability for decay by alpha emission. The possibility of observing such a continuum was mentioned by Cheifetz *et al* (2). The $^{143}Nd(n,\alpha)^{140}Ce$ reaction is ideally suited to the study of the $(n,\gamma\alpha)$ reaction because of the large energy difference (1.6 MeV) between the ground state and first excited state and because of the large (n,α) cross section (~22 mb)

for the ground state transition.

In the measurements of the energy correction factor, K , described in Chapter III the spectrum was obtained from a mixed ^{226}Ra - ^{228}Th source. A portion of this spectrum is shown in Figure 19 to show the measured line shape for a monoenergetic alpha transition.

One can derive an expression for the shape of the $(n,\gamma\alpha)$ spectrum as follows. The partial radiation width for electric radiation of order ℓ between a level at energy E_a, and one of energy E_b, by a gamma ray of energy $E_\gamma = E_a - E_b$ is given by (51)

$$\left\langle \Gamma_{E\ell}(E_a,E_b) \right\rangle_{av} \sim C_\ell E^{2\ell+1} D_\ell(E_a) \qquad 7.1$$

where

$$C_\ell = \frac{18(\ell+1)(2\ell+1)}{\ell(\ell+3)^2 \left[(2\ell+1)!!\right]^2} \frac{e^2}{\hbar c} \frac{1}{D_o} \left[\frac{R}{\hbar c}\right]^{2\ell} \quad . \qquad 7.2$$

In these expressions R is the nuclear radius, e, $\hbar$, and c have the usual meanings and ℓ is the multipolarity of the gamma radiation. Since only the dipole, $\ell = 1$, term contributes significantly (54,55) other values of ℓ will be ignored (as well as magnetic radiation) in the discussion which follows. The level spacing, $D_\ell(E)$,(for levels of the same spin and parity) can be given by (52)

$$D_\ell(E) = D_o \exp\left(-2\sqrt{aE}\right) \qquad 7.3$$

where D_o is the level spacing at the ground state and a determines the rate of change of the level spacing with energy. For E1 radiation, then , the partial radiation width is given by

$$\Gamma_{E1}(E_a,E_b) = C E^3 D(E_a) \quad . \qquad 7.4$$

Figure 19: ^{214}Po Alpha Spectrum

The line shape of a monoenergetic alpha transition is shown. The ^{214}Po peak (7.68 MeV) spectrum was obtained using a large area source and the electrostatic particle guide.

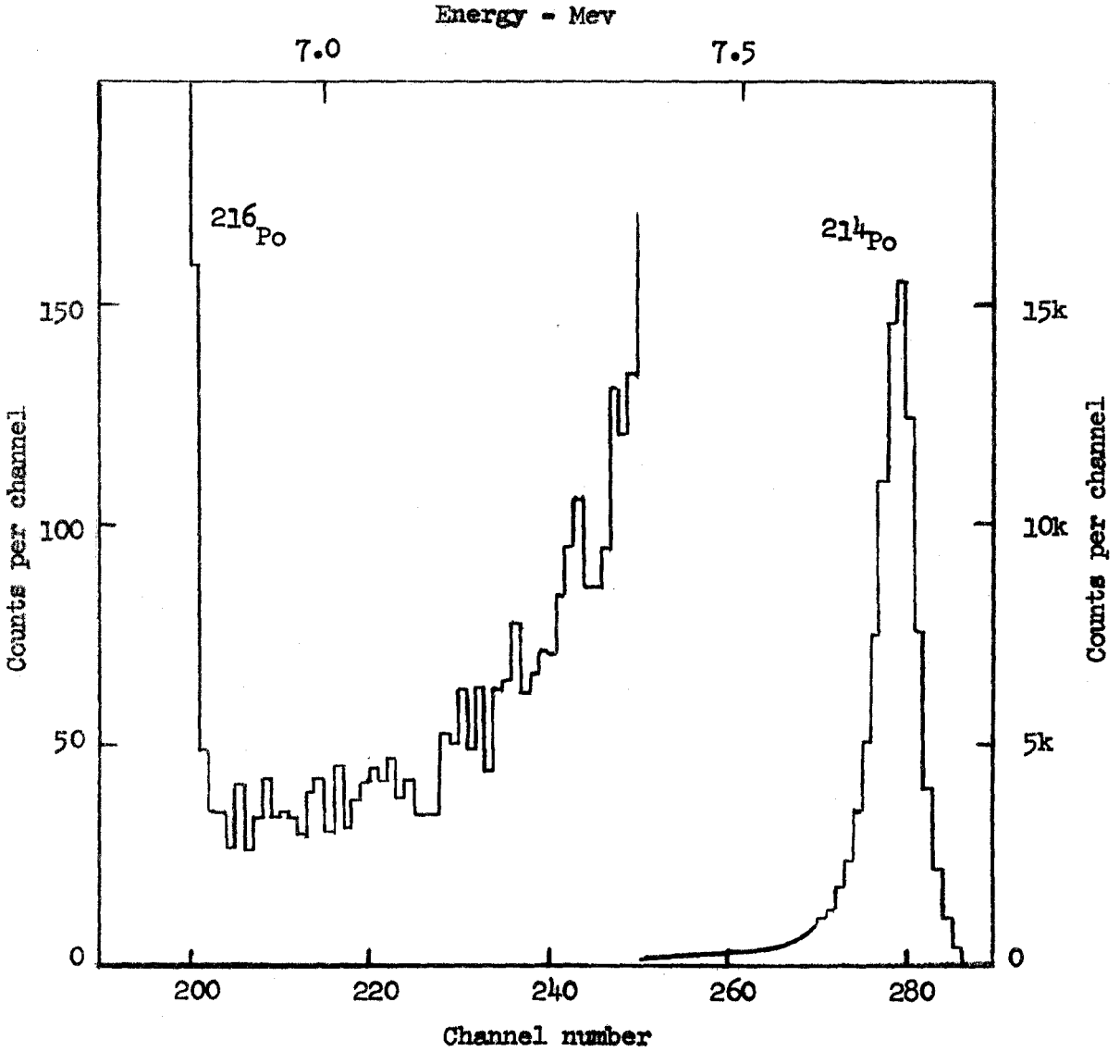
Energy - Mev
7.0
7.5
216Po
214Po
150
100
50
0
15k
10k
5k
0
Counts per channel
Counts per channel
200
220
240
260
280
Channel number

From equation (7.3) and (7.4) one obtains the total radiation width for gamma decay for a level at energy E_a. It is given by

$$\Gamma_{tot}(E_a) = C \int_0^{E_a} E^3 \frac{D(E_a)}{D(E_a - E)} dE \quad . \qquad 7.5$$

The radiation width for alpha emission from a level at energy E_a is given by the expression,

$$\Gamma_\alpha(Q_a) = \delta^2(Q_a)\, P_L(Q_a) / 2\pi \qquad 7.6$$

where δ^2 is the reduced width and P_L is the penetrability. Q_a specifies the Q-value for alpha decay of a level in the parent at an excitation energy E_a. Equation (7.6) considers only alpha emission to the ground state of the daughter nucleus and hence only one value of P_L need be considered (for even-even nuclei).

In the particular case of the reaction $^{143}Nd\ (n,\alpha)\ ^{140}Ce$, the capture state has $J^\pi = 3^-$ and alpha decay to the ground state has $L = 3$. E1 gamma emission from the capture state populates levels with $J^\pi = 2^+, 4^+$ which can alpha decay to the ground state of ^{140}Ce.

The probability for gamma emission from the capture state at energy E_n to a level at energy $E_n - E_\gamma$ is given by

$$P_\gamma(E_n, E_\gamma) = \frac{\Gamma_{E1}(E_n, E_n - E_\gamma)}{\Gamma_{tot}(E_n)} \quad . \qquad 7.7$$

The probability of a gamma of energy E_γ to $E_\gamma + dE_\gamma$ is then

$$N_\gamma(E_n, E_\gamma)dE = \frac{\Gamma_{E1}(E_n, E_n - E_\gamma)}{\Gamma_{tot}(E_n)} \frac{1}{D(E_n - E_\gamma)} dE_\gamma \quad . \qquad 7.8$$

From equation (7.6) the level at energy (E_n-E_γ) has a probability of alpha decay given by

$$P_\alpha(E_n-E_\gamma) = \frac{\Gamma_\alpha(Q_n-E_\gamma)}{\Gamma_{tot}(E_n-E_\gamma)} \quad . \qquad 7.9$$

Thus the probability of alpha decay following gamma emission is obtained by combining equations (7.6), (7.8), and (7.9). This gives

$$N_\alpha(Q_n-E_\gamma)dE_\gamma = \frac{\Gamma_{El}(E_n,E_n-E_\gamma)}{\Gamma_{tot}(E_n)} \frac{1}{D(E_n-E_\gamma)} \frac{\delta^2(Q_n-E_\gamma)\ P(Q_n-E_\gamma)}{2\pi\Gamma_{tot}(E_n-E_\gamma)} dE_\gamma \qquad 7.10$$

where

$$P(Q_n-E_\gamma) = P_2(Q_n-E_\gamma) + P_4(Q_n-E_\gamma) \quad . \qquad 7.11$$

The ratio of the number of alphas per unit energy which arise from the $(n,\gamma\alpha)$ reaction, to the number from the capture state, R(E), is then given by

$$R(E)dE = \frac{P(Q_n-E_\gamma)}{P_3(Q_n)} \frac{\delta^2(Q_n-E_\gamma)}{\delta^2(Q_n)} \frac{\Gamma_{El}(E_n,E_n-E_\gamma)}{\Gamma_{tot}(E_n-E_\gamma)} \frac{dE_\gamma}{D(E_n-E_\gamma)} \quad . \qquad 7.12$$

Using equations (7.3), (7.4) and (7.5) this becomes

$$R(E)dE = \frac{P(Q_n-E_\gamma)}{P_3(Q_n)} \frac{\delta^2(Q_n-E_\gamma)}{\delta^2(Q_n)} \frac{\exp\left\{-2\sqrt{aE_n}\left[1-2\sqrt{1-E_\gamma/E_n}\right]\right\}E_\gamma^3\, dE_\gamma}{\left[\int_0^{E_n-E_\gamma} \exp\left[-2\sqrt{a((E_n-E_\gamma)-E)}\right] E^3\, dE\right]}$$

$$7.13$$

At this point it is worthwhile to consider the validity of this equation in terms of the assumptions used to derive it. The use of

equations (7.3) and (7.4) to calculate Γ_γ gives only fair agreement with experiment by appropriate choices of D_o and a. In equation (7.12), however, D_o cancels out and only the parameter, a , remains in the level spacing formula. Because ratios have been taken, the uncertainty due to a poor knowledge of the exact form of the expression for $\langle \Gamma_{E\gamma}(E_a,E_b) \rangle_{av}$ and the uncertainty due to using only $\ell = 1$ should cancel out.

Equation (7.13) was evaluated using values of E_γ from 0 to 1.6 MeV at intervals of 0.1 MeV using the value, a = 8.9 , and assuming that $\delta^2(Q_n-E_\gamma)/\delta^2(Q_n) = 1$. The value, a , was obtained from a linear interpolation between the values of a = 8.0 for A = 115 , and a = 10.0 for A = 181 [53]. The equation was recalculated for values of a = 8.0 and a = 10.0 to show the small dependence on a. Figure 20 shows the calculated spectrum for the three values of a, where R(E)dE is plotted versus the alpha energy. On the same graph are plotted the experimental values which were obtained from the spectrum of Figure 14 by subtracting off a reasonable background due to tailing from the source thickness. The error bars include the uncertainty in the background (~10%) and the statistical uncertainties.

The calculated spectrum is lower than the experimental one and not the same shape. It is felt, however, that the assumption that the reduced width is constant is not good. Since the δ^2 for the ground state is about 10^5 times as large as δ^2 for the capture state it is reasonable to expect that $\delta^2(Q_n-E_\gamma)$ has some energy dependence. This was taken to be of the form

$$\delta^2(E) = \delta_o^2 \exp(-2\sqrt{bE}) \qquad 7.14$$

Figure 20: $(n,\gamma\alpha)$ Spectrum

The experimental (⧫) and calculated $(n,\gamma\alpha)$ spectrum is shown; b = 0 and 1) a = 8.0 (■), 2) a = 8.9 (▼), 3) a = 10.0 (●).

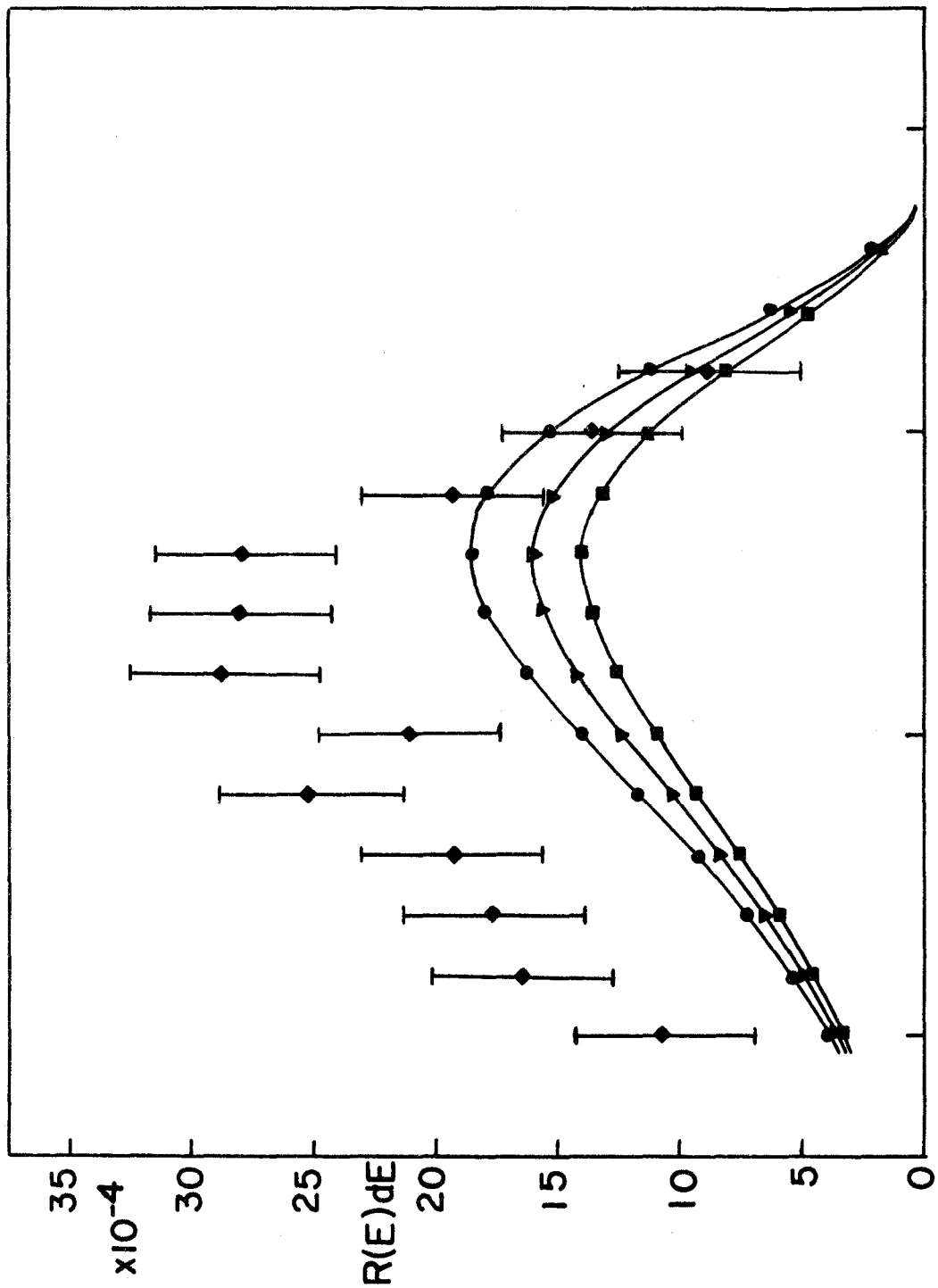
R(E)dE
x10⁻⁴
35
30
25
20
15
10
5
0
8.0
8.5
9.0
9.5
Alpha energy - MeV

where E is the excitation energy, δ_o^2 is the ground state alpha reduced width, and b is determined from the measured alpha reduced width for the capture state. Using $\delta_o^2 = 223$ keV [56] and $\delta^2(7.83) = 12.4$ eV one obtains a value $b = 3.07$.

Using this value R(E)dE was recalculated for $a = 8.9$. This curve, which is shown in Figure 21, agrees remarkably well with the experimental data.

7.3 Alpha Reduced Widths

For all observed transitions studied in the (n,α) reactions, alpha reduced widths, δ_{exp}^2 , have been determined. It is of interest to relate these to a nuclear model. A successful model will give agreement between measured and calculated reduced widths for different nuclei- in particular for transitions to the ground state or first excited state. It will also give an understanding of the fluctuations in reduced widths to various levels of the same daughter nucleus.

The problem of comparing reduced widths for various nuclei will be discussed first. From the statistical model, the radiation width for alpha decay can be expressed as

$$\Gamma_\alpha = \frac{D}{2\pi} P_L \quad , \qquad 7.15$$

where D is the average level spacing and P_L is the penetrability. Since $\delta_{exp}^2 = \lambda h/P$ one can obtain an expression for the reduced width as follows

$$\delta^2 = \delta_o^2 \, D/D_o \quad , \qquad 7.16$$

where δ_o^2 is the reduced width for ground state alpha decay and D_o is the level spacing near the ground state (and is typically taken to be 1 MeV).

Figure 21: $(n,\gamma\alpha)$ Spectrum

The experimental (⧫) and calculated $(n,\gamma\alpha)$ spectrum is shown; b = 3.07 and a = 8.9 (●).

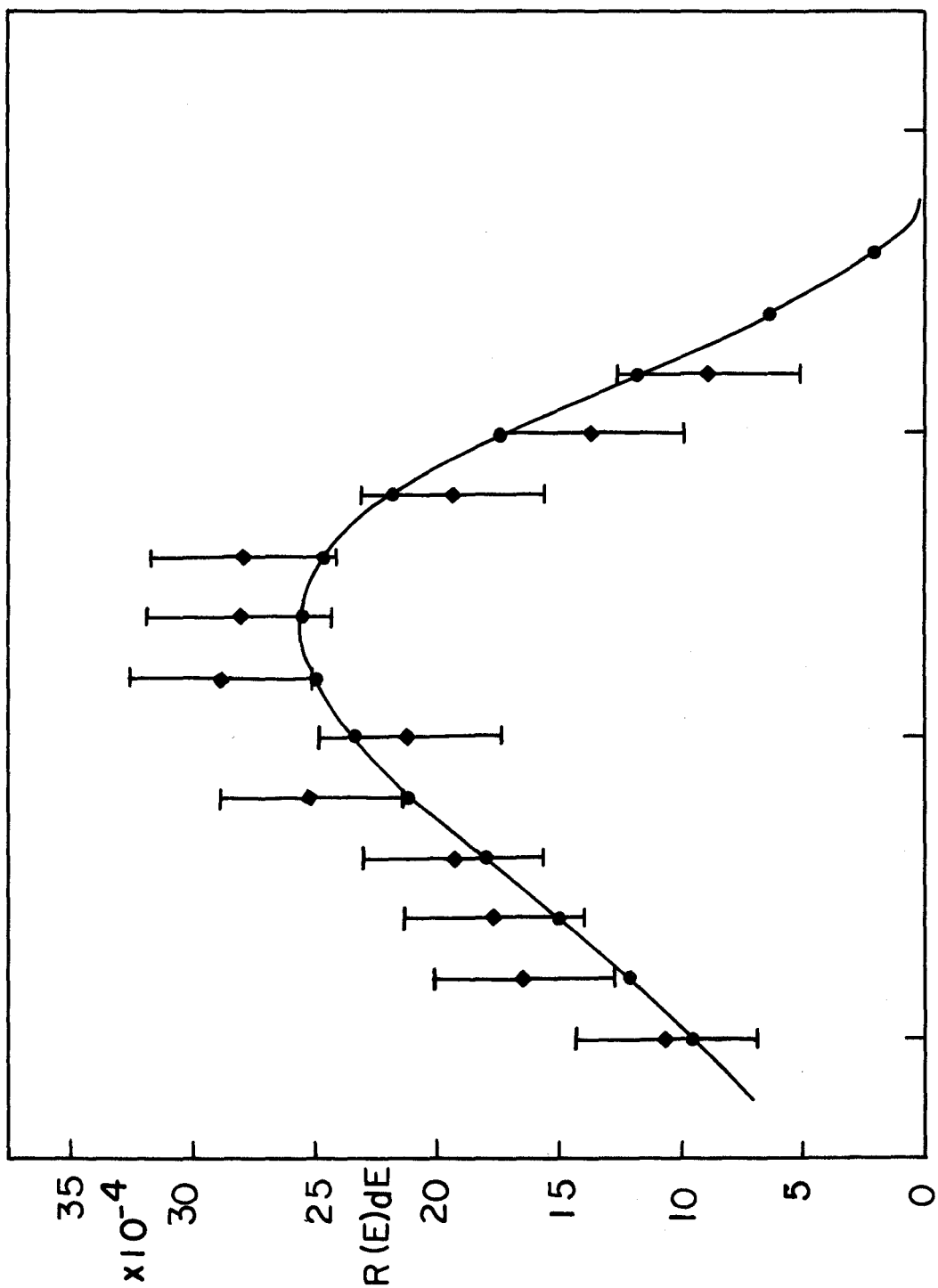
35
30
25
20
15
10
5
0
x10⁻⁴
R(E)dE
8.0
8.5
9.0
9.5
Alpha energy - MeV

Using known values of δ_o^2 (or 100 keV if the value is unknown) and measured values of D one can obtain an estimate of δ^2 for alpha decay from the capture state. These values are shown in Table 7.1 along with the experimental values for ^{149}Sm, ^{147}Sm and ^{143}Nd.

In general the agreement is satisfactory. The only exception is the experimental reduced width for the transition to the ground state of ^{144}Nd. This value is quite low. It was determined by considering a capture cross section of 75 ± 11 barns determined by Simpson et al [49]. It was assumed that this was due to a 3^- level. However, the only known level with $J^\pi = 3^-$ is at 3.4 eV. Evaluating the Breit-Wigner formula at 0.026 eV for this level using the parameters obtained by Poortmans et al [47] one finds a contribution of only 3.2 barns. The resonance at 18.3 eV with $J^\pi = 4^-$ contributes 4.2 barns. Assuming that a 4^- bound level is contributing the major portion of the capture cross section (ie 67 b) one obtains a value $\delta^2 = 4.4$ eV for the alpha decay to the ground state of ^{144}Nd. This is in agreement with the results for ^{149}Sm and ^{143}Nd which have similar reduced widths for the transitions to the ground state and first excited state.

It is interesting that an experimentally determined level spacing, D, can be used to estimate reduced widths. It gives some experimental verification of the periodic motion of the nucleus at high excitation.

The alpha reduced widths for decay from the capture state to various levels in the daughter nucleus show fluctuations from level to level as well as the the differences in alpha reduced widths from nuclide to nuclide. In the case of ^{149}Sm there are variations in the reduced width for levels up to about 1.6 MeV. Above this there are several

Table 7.1

Calculated Alpha Reduced Widths

Target	δ_o^2	D_o	D	δ_{calc}^2	δ_{exp}^2 g.st.	δ_{exp}^2 1^{st} ex.
^{149}Sm	100 keV	1.0 MeV	6.6 eV	0.83 eV	1.12 eV	2.22 eV
^{147}Sm	100	1.0	14	1.74	0.19 (4.4)	1.38
^{143}Nd	223	1.0	33	7.36	12.4	5.0

transitions that appear to be enhanced by about a factor of 5. Since spins and parities are not known, however, the actual reduced widths may differ from those listed in Table 4.1 by as much as a factor of 2. The neutron pairing energy for ^{146}Nd is about 2 MeV (57). This suggests that these levels may have a large 1-particle-1-hole component which could enhance the transition from the multi-particle-hole capture states.

Only four alpha transitions have been observed from the capture states of ^{148}Sm to the levels in ^{144}Nd. The spins and parities are known for these levels. There is, however, some uncertainty about which of the capture states are contributing to the ground state (n,α) cross section. The alpha reduced widths in this case are fairly constant.

For these two cases there is little that can be done at the present time in trying to calculate alpha reduced widths. Not only is the wavefunction for the capture state unknown, but as well, the nature of the levels in ^{146}Nd and ^{144}Nd is not known.

On the other hand, for the ^{143}Nd (n,α) ^{140}Ce reaction, the spins and parities of the levels of ^{140}Ce are known. As well, studies of the levels have been made theoretically by Rho (41) and experimentally by Baer *et al* (43). The alpha reduced widths of this reaction are discussed below.

Rho (41,59) has discussed the level scheme of ^{140}Ce in terms of two quasiparticle levels. He calculates the wavefunctions for most of the levels found in our (n,α) studies of ^{143}Nd . Experimental studies (43) tend to verify his calculations.

Mang's equation for the reduced width, γ_L, of equation (1.6) involves integration over the coordinates of the nucleons of the daughter and relative coordinates of the four nucleons of the alpha particle. Using the delta-function approximation for the alpha particle [5,15,58] a great deal of simplification can be achieved. It has been shown that even with this approximation good relative decay rates can be obtained [58].

The equations of pertinence here are summarized as follows. For alpha decay of the form $\left[(j_p)^1(j_p)^1\right]_L (j_n)^2_o$ core$\leftrightharpoons$core the expression for the amplitude, γ_L, is given by

$$\gamma_L = \text{Const } (-1)^{l_n + j_n - \frac{1}{2}} \left[\frac{(2j_n+1)(2j_p+1)(2j_p'+1)}{2L+1}\right]^{\frac{1}{2}} x$$
$$x\ (j_p j_p' \tfrac{1}{2} -\tfrac{1}{2} | L0)\ R_n^2\ R_p\ R_{p'}\ B_n\ B_{p'} \qquad 7.17$$

where j_n, j_p, l_n and l_p specify the nucleon orbitals and L is the relative angular momentum. The values B_n and $B_{p'}$ correct the reduced width amplitudes for an overestimate of γ for high j orbitals. They are given by

$$B_n = \exp\left[-\,0.013\ l_n(l_n+1)\right] \qquad 7.18$$

and

$$B_{p'} = \exp\left(-\,0.0065\left[l_p(l_p+1) + l_{p'}(l_{p'}+1) - \tfrac{1}{2}L(L+1)\right]\right) . \qquad 7.19$$

The quantities R_n and R_p are values of nucleon wavefunctions evaluated at the chosen connection radius R_o. One may use three dimensional harmonic oscillator functions or the numerical wavefunctions calculated by Blomqvist et al [59].

Equation (7.17) could be used if the capture state were 0^+ and under the assumption that the capture state configuration is similar to the daughter plus two protons and two neutrons. Corrections to the theory can be made to calculate branching ratios to the levels in ^{140}Ce and these will be carried out in the future.

CHAPTER VIII

CONCLUSIONS

Fine structure in thermal neutron (n,α) reactions has been studied for targets ^{149}Sm, ^{147}Sm, and ^{143}Nd. The investigation of alpha decay from thermal neutron capture states to levels in the daughter nucleus up to excitation energies of 2 to 3 Mev was made possible by a new device, called an electrostatic particle guide.

This device consists of a long cylinder with a central electrode held at a negative potential of 30 to 50 kV. It focusses and directs alpha particles from a target in the intense neutron flux of the thermal column of a reactor (which is a region of high background) to a low background region in the room where they are detected. The use of this technique which solves the problems of background and low energy tailing has been amply justified by the wealth of fine structure data that has been obtained.

The electrostatic particle guide technique has been described in detail and equations derived which express the collection efficiency in terms of the parameters and dimensions of the device. The validity of these equations has been investigated and verified experimentally.

From the reaction studies, accurate alpha energies and cross sections have been determined for each transition. Level schemes for ^{146}Nd, ^{144}Nd, ^{140}Ce have been obtained with good agreement with previous results obtained by other methods. Several new levels were found in ^{146}Nd.

In the ^{143}Nd (n,α) ^{140}Ce reaction study, evidence has been seen for the much less intense reaction ^{143}Nd (n,γα) ^{140}Ce. The shape of this continuum of alpha particles depends on the level spacing and the energy dependence of the reduced width. The spectrum has been calculated assuming dipole radiation from the capture state to be predominant, and assuming that the reduced width depends on the level spacing. The experimental spectrum is in good agreement with the calculated one. The total (n,γα) intensity is found to be $\leqslant 2\%$ of the total intensity of the capture state to ground state transition.

Experimental alpha reduced widths have been calculated and discussed in detail. The variation in δ^2 from nucleus to nucleus can be understood on the basis of the statistical model and depends on the level spacing at the neutron binding energy. The levels in ^{140}Ce can be described adequately as two quasiparticle levels and it is found experimentally that alpha transitions to levels of the same configuration (ie $(g_{7/2}^2)_{J=0,2,4}$) have similar alpha reduced widths. The transitions to the levels with a predominant $(d_{5/2}^2)_J$ configuration are enhanced by an order of magnitude over levels with a predominant $(g_{7/2}^2)_J$ configuration.

APPENDIX I

DETAILS OF THE CALCULATION OF THE FRACTION OF PARTICLES STRIKING THE WIRE

The angle of the acceptance cone is defined by equation (2.8):

$$\beta_{max} = A/\left(\sqrt{1 - (r_o/R)^2 \sin^2\phi}\right) \qquad \text{A1.1}$$

where

$$A^2 = \frac{|qV_o|}{E_a}\frac{\ln(R/r_o)}{\ln(R/s)} \quad . \qquad \text{A1.2}$$

Since β is small, the end of the acceptance cone on a unit sphere is an ellipse defined in polar coordinates (β , ϕ) by equation (A1.1) as shown in Figure 22 . The solid angle of the acceptance cone lost to particles striking the wire is then the shaded area shown in Figure 22 whose boundaries are β_{max} and ϕ_{min} . The latter is given by equation (2.14) as follows

$$\phi_{min} = \sin^{-1}\left((s/r_o)\sqrt{1 + k^2/\beta^2}\right) \qquad \text{A1.3}$$

where

$$k^2 = \frac{|qV_o|}{E_a}\frac{\ln(r_o/s)}{\ln(R/s)} \quad . \qquad \text{A1.4}$$

Transforming to cartesian coordinates $x = \beta\cos\phi$, and $y = \beta\sin\phi$ one obtains

$$y = R\sqrt{\frac{A^2 - x^2}{R^2 - r_o^2}} \qquad \text{A1.5}$$

in place of β_{max} . Similarily, ϕ_{min} becomes

$$y = s\sqrt{\frac{x^2 + k^2}{r_o^2 - s^2}} \quad . \qquad \text{A1.6}$$

FIGURE 22: Collection Cone

The end of the collection cone on the surface of a unit sphere is shown with shaded areas indicating the part lost to particles striking the wire.

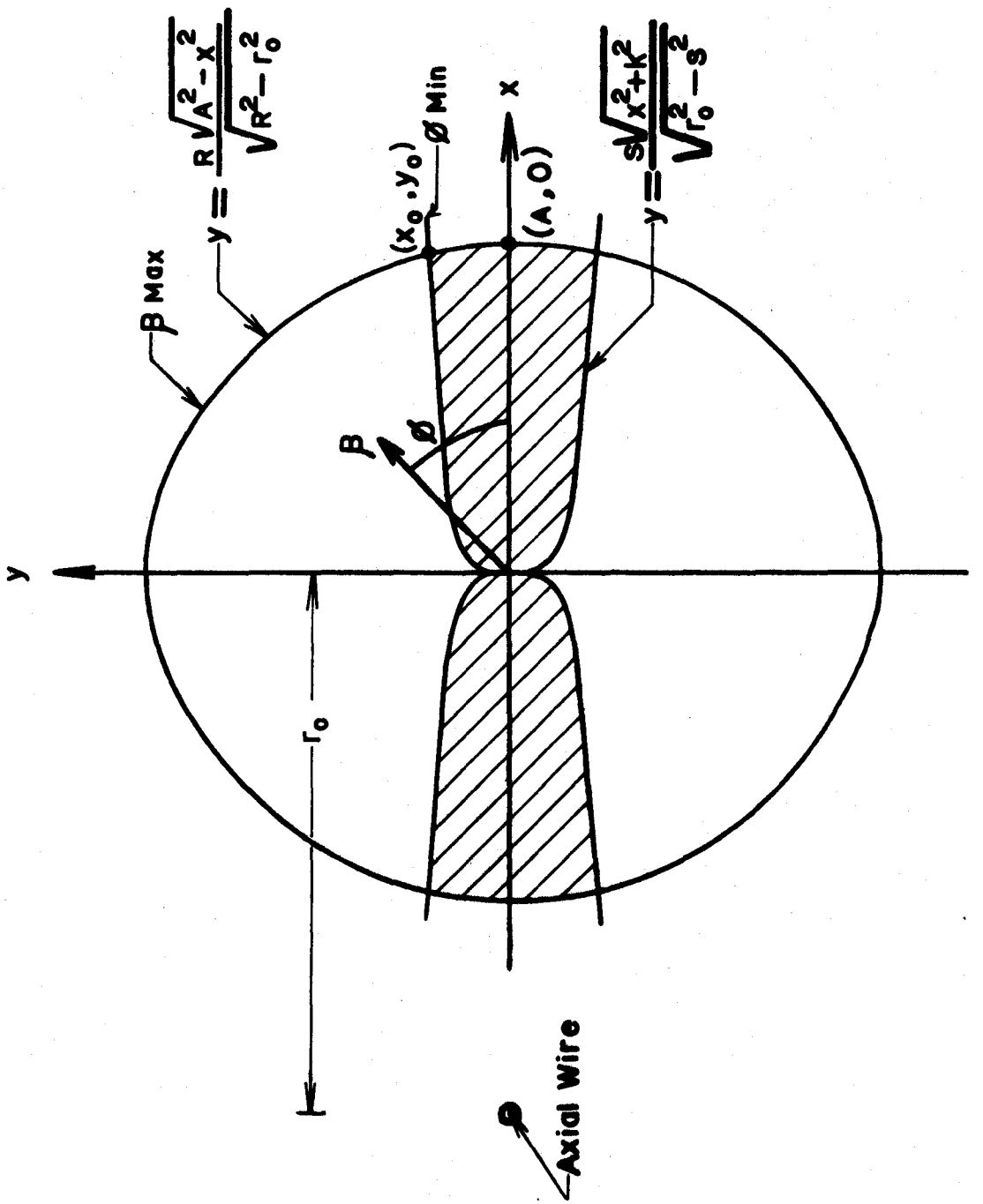
β Max
$y = \frac{R\sqrt{A^2-x^2}}{\sqrt{R^2-r_o^2}}$
(x_o, y_o)
ø Min
x
(A, O)
$y = \frac{s\sqrt{x^2+k^2}}{\sqrt{r_o^2-s^2}}$
β
ø
y
r_o
Axial Wire

Thus the solid angle , $A_w(r_o)$, lost to particle striking the wire for a point source at a radius r_o is given by

$$A_w(r_o) = 4\left[\int_0^{x_o} s\sqrt{\frac{x^2+k^2}{r_o^2-s^2}}\,dx + \int_{x_o}^{A} R\sqrt{\frac{A^2-x^2}{R^2-r_o^2}}\,dx\right] . \quad \text{A1.7}$$

Now

$$\int\sqrt{x^2+k^2}\,dx = (x/2)\sqrt{x^2+k^2} + (k^2/2)\ln\left(x+\sqrt{x^2+k^2}\right) \quad \text{A1.8}$$

$$\int\sqrt{A^2-x^2}\,dx = (x/2)\sqrt{A^2-x^2} + (A^2/2)\sin^{-1}(x/A) \quad \text{A1.9}$$

Combining (A1.8) and (A1.9) with (A1.7) gives

$$A_w(r_o) = \frac{2s}{\sqrt{r_o^2-s^2}}\left[x_o\sqrt{x_o^2+k^2} + k^2\ln\left(x_o+\sqrt{x_o^2+k^2}\right) - k^2\ln(k)\right]$$

$$+ \frac{2R}{\sqrt{R^2-r_o^2}}\left[A^2\sin^{-1}(1) - x_o\sqrt{A^2-x_o^2} - A^2\sin^{-1}(x_o/A)\right] \quad \text{A1.10}$$

where

$$x_o = \sqrt{\frac{R^2A^2(r_o^2-s^2) - s^2k^2(R^2-r_o^2)}{r_o^2(R^2-s^2)}} . \quad \text{A1.11}$$

The fraction of particles from a point source at a radius r_o which strike the wire is given by

$$F_w(r_o) = A_w(r_o)/4\pi . \quad \text{A1.12}$$

Under the assumptions that $R \gg s$ and that $r_o \geq 10s$, equation (A1.11)

reduces to $x_o = A$ and one obtains

$$F_w(r_o) = \frac{s\,|qV_o|}{2\pi r_o E_a}\left[\sqrt{\frac{\ln(R/r_o)}{\ln(R/s)}} + \frac{\ln(r_o/s)}{\ln(R/s)}\ln\left[\frac{\sqrt{\ln(R/r_o)} + \sqrt{\ln(R/s)}}{\sqrt{\ln(r_o/s)}}\right]\right] . \qquad \text{A1.13}$$

which is identical to equation (2.16).

For an extended source of radius b, the fraction of particles which strike the wire is given by

$$F_w = (2/(b^2-s^2))\int_s^b F_w(r_o)\; r_o\; dr_o \quad . \qquad \text{A1.14}$$

For a particular size of target the correction factor for particles lost to the wire is conveniently expressed as the ratio of the fraction of particles which strike the wire, equation (A1.14), to the fraction of particles which achieve a bound orbit, equation (2.10),

$$R_h = F_w \,/\, F_c \quad . \qquad \text{A1.15}$$

APPENDIX II

DETAILS OF THE RADIAL DISTRIBUTION CALCULATION

The solution of differential equations by analogue techniques is well known. In the MIMIC programming system[50] for the IBM 7040 computer an analogue computer is simulated by providing a number of operational elements such as adders, integrators and multipliers. These are interconnected in the program in a way similar to the interconnection of the elements of an analogue computer but without the problems of time and amplitude scaling. The solution to the differential equation can be printed out at preselected equal time intervals.

The equations of motion for a particle in the electrostatic particle guide are given by equations (2.22) and(2.23) :

$$\ddot{r} = A_1/r^3 + A_2/r \qquad \text{A2.1}$$

and

$$\dot{\theta} = C/r^2 \qquad \text{A2.2}$$

where

$$A_1 = r_o^2 v_p^2 \sin^2\phi \quad , \qquad \text{A2.3}$$

$$A_2 = (|qVo|)/ m \ln(s/R) \quad , \qquad \text{A2.4}$$

and

$$C = A_1^{\frac{1}{2}} \quad . \qquad \text{A2.5}$$

At $t = 0$, the initial conditions are $r = r_o$, $\dot{r} = v_p \cos\phi$, and $\theta = 0$ (where $v_p = \beta (2E_a/m)^{\frac{1}{2}}$). The symbols are defined in Chapter 2 . The block diagram representing the solution of these equations is shown in Figure 23 .

Figure 23 : Solution of Orbit Equations

The block diagram is shown for the solution of the equations of motion of a charged particle in a logarithmic potential.

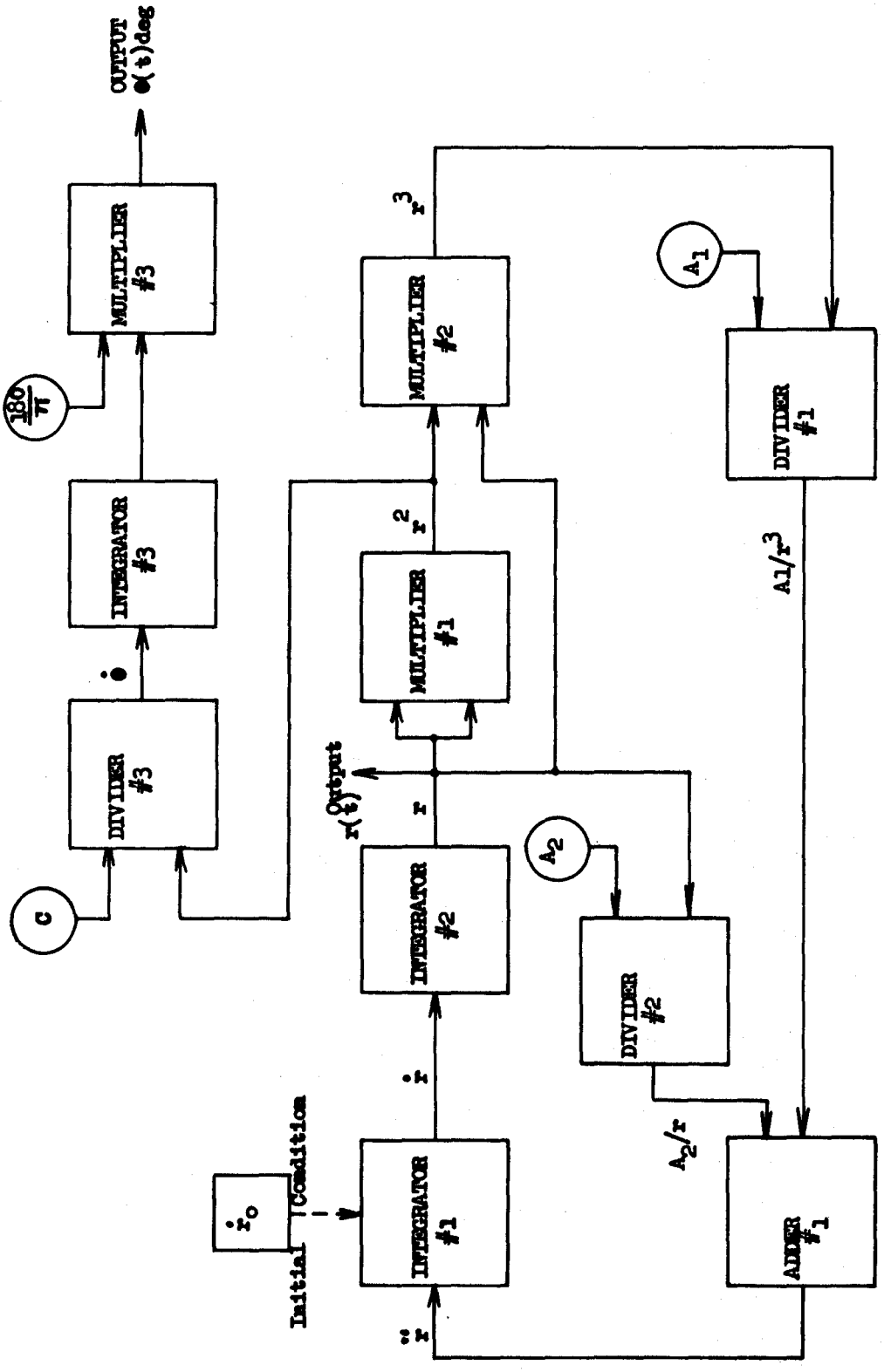
OUTPUT
θ(t)deg
MULTIPLIER #3
INTEGRATOR #3
DIVIDER #3
MULTIPLIER #2
MULTIPLIER #1
INTEGRATOR #2
INTEGRATOR #1
DIVIDER #2
DIVIDER #1
ADDER #1
180/π
C
A1
A2
r(t) Output
Initial Condition
A1/r3
A2/r

The particle radial distribution function for a point source is given by $g(r_o,r_d)$ which is normalized to unity and specifies the fraction of particles between r_d and $r_d + dr_d$ at the detector end for a point source at radius r_o from the axis. Consider an extended source of radius R, emitting N_o particles/cm^2/sec isotropically in angle. The radial density function, $\rho(r_d)$, which gives the number of particles /cm^2/sec at a radius r_d, is given by

$$\rho(r_d)\, dr_d = \frac{1}{2\pi r_d} \int_s^R g(r_o,r_d) \left[F(r_o) - F_w(r_o) \right] 2\pi r_o N_o dr_o \qquad \text{A2.6}$$

where $F(r_o)$ is the point source collection efficiency formula given by equation (2.9). $F_w(r_o)$ corrects for particles striking the wire and is given by equation (2.16).

The first step in the calculation of $\rho(r_d)$ was to determine the radial distribution function, $g(r_o,r_d)$, for a point source at radius r_o. This was done by dividing the acceptance cone into about 180 segments of equal solid angle, each charactarized by a value of β and ϕ. A trajectory was determined for each of these 180 values of β and ϕ using the MIMIC program and the radius, r_d, at which the particle left the cylinder was obtained. The distribution, $g(r_o,r_d)$, normalized to unity, is then given by

$$g(r_o,r_d) = \frac{\text{The Number of Particles Between } r_d \text{ and } r_d + \delta r_d}{N_c(r_o)}$$

$$= \frac{N(r_o,\, r_d)}{N_c(r_o)} \qquad \text{A2.7}$$

where $N_c(r_o)$ is the number of trajectories calculated at a radius r_o. This distribution was determined for values of r_o from 0.5cm to 3.5 cm in 0.5 cm increments for a 2.74 MeV triton with V_o = 20 kV , s = 0.025 cm and R = 3.75 cm . The radial density function , $\rho(r_d)$, was then determined by numerically integrating equation (A2.6) and using the value of N_o determined from the intensity of the 2.74 MeV triton group with no voltage on the wire. Table A.1 lists the data used in obtaining the function, $\rho(r_d)$, and Figure 7 shows the calculated values of $\rho(r_d)$ plotted along with four values determined experimentally. The agreement is very good.

TABLE A.1

Values of $N(r_o, r_d)$ Used to Obtain $\rho(r_d)$

r_d cm	r_o cm						
	0.5	1.0	1.5	2.0	2.5	3.0	3.5
0-0.5	50	15	8	2	3	2	1
0.5-1.0	64	46	19	14	11	7	8
1.0-1.5	46	53	46	22	18	6	17
1.5-2.0	0	31	50	43	23	22	28
2.0-2.5	7	28	23	41	33	34	25
2.5-3.0	13	7	23	29	55	46	34
3.0-3.5	0	0	5	26	29	43	30
3.5-3.75	0	13	15	8	10	17	25
$N_c(r_o)$	180	193	189	185	182	177	168
$F(r_o)$	8.40×10^{-4}	5.07	3.67	2.68	2.00	1.33	0.68
$F_w(r_o)$	0.87×10^{-4}	0.27	0.16	0.10	0.07	0.04	0.02

REFERENCES

(1) R. D. Macfarlane and I. Almodovar, Phys. Rev., 127 (1962) p.1665.

(2) E. Cheifetz, J. Gilat and A. I. Yavin, Phys. Letters, 1 (1962) p.289.

(3) G. Gamow, Z. Physik, 51 (1928) p.204.

(4) E. U. Condon and R. W. Gurney, Nature, 122 (1928) p. 439.

(5) P. J. Brussaard and H. A. Tolhoek, Physica, 24 (1958) p. 263.

(6) G. Igo and R. M. Thaler, Phys. Rev., 106 (1957) p.126.

(7) G. H. Winslow, Phys. Rev., 96 (1954) p.1032.

(8) R. G. Thomas, Progr. Theoret. Phys., 12 (1954) p.253.

(9) H. J. Mang, Phys. Rev., 119 (1960) p.1069.

(10) H. J. Mang, Ann. Rev. Nucl. Sci., 14 (1964) p.1 .

(11) J. O. Rasmussen, Phys. Rev., 113 (1959) p.1593.

(12) J. O. Rasmussen, Alpha-,Beta-, Gamma-Ray Spectroscopy, vol. 1, North-Holland Publ. Co. (1965) p.701.

(13) H. J. Mang and J. O. Rasmussen, Kgl. Danske Videnskab. Selskab, Mat.-Fys. Skrifter 2 , No. 3 (1962).

(14) J. K. Poggenburg, UCRL-16187, Thesis, University of California (1965) unpublished.

(15) D. H. Wilkinson, Proceedings of the Rutherford Jubilee International Conference , Heywood and Co. Ltd. (1961) p.339.

(16) K. Harada, Progr. Theoret. Phys., 27 (1962) p.430.

(17) Gy. Bencze and A. Sandulescu, Phys. Letters, 22 (1966) p.473.

(18) R. D. Griffioen, UCRL-9566 (1961) unpublished p. 147

(19) J. M. Blatt and V. F. Weisskopf, Theoretical Nuclear Physics, John Wiley and Sons (1952) p.386.

(20) D. J. Hughes and R. B. Schwartz, Neutron Cross Sections, BNL-325 and Supplements, 2nd edition (1958).

(21) V. N. Andreev and S. M. Sirotkin, J. Nucl. Phys.(U.S.S.R.), 1 (1965) p.252.

(22) W. E. Waters, Motion of electrons between concentric cylinders, Diamond Ordinance Fuse Laboratories Techn. Rep. no. 525(1957).

(23) R. H. Hooverman, J. Appl. Phys.,34 (1963) p.3505 .

(24) R. G. Herb, T. Pauly and K. J. Fisher, Bull. Am. Phys. Soc.,8 (1963) p.336 .

(25) A. Ghiorso and R. Main, unpublished results (1963)

(26) G. D. O'Kelley, Applications of Computers to Nuclear and Radiochemistry , NAS-NS 3107, Office of Technical Services,USA(1962) p.67 .

(27) A. H. Wapstra, Nucl. Phys.,57 (1964) p.48.

(28) K. Beg, private communication (1967).

(29) G. Igo, Phys. Rev. Letters,1 (1958) p.72 .

(30) D. J. Buss, E. G. Funk and J. W. Mihelich, Phys. Rev.,141 (1966) p.1193 .

(31) A. V. Ramayya and Y. Yoshizawa, Phys. Rev.,137 (1965) p.B13.

(32) K. Beg and R. D. Macfarlane, Bull. Am. Phys. Soc.,10 (1965) p.724.

(33) F. Poortmans, H. Ceulemans, J. A. Deruytter and M. Nève de Mévergnies, Nucl. Phys.,82 (1966) p.331 .

(34) M. Dakowski, T. Krogulski, E. Piekarz and M. Sowinski, Nucl. Phys., A97 (1967) p.187 .

(35) H. Marshak and V. L. Sailor, Phys. Rev.,109 (1958) p.1219 .

(36) B. N. Brockhouse, Can. J. Phys.,31 (1953) p.432 .

(37) L. D. Roberts, S. Bernstein, J. W. T. Dabbs and C. P. Stanford, Phys. Rev.,95 (1954) p.105 .

(38) H. Marshak, H. Postma, V. L. Sailor and C. A. Reynolds, Bull. Am. Phys. Soc.,6 (1961) p.418 .

(39) N. J. Pattenden, Proceedings of the Second United Nations International Conference of the Peaceful Uses of Atomic Energy, Geneva, (1958) vol. 16, p.44 .

(40) W. R. Daniels and D. C. Hoffman, Bull. Am. Phys. Soc.,9 (1964) p. 562 .

(41) M. Rho, Nucl. Phys.,65 (1965) p.497 .

(42) H. Hay, J. Nucl. Energy, 7 (1958) p.199 .

(43) H. W. Baer, J. J. Reidy and M. L. Wiedenbeck, Nucl. Phys.,86 (1966) p.332 .

(44) J. E. Monahan, S. Raboy and C. C. Trail, Phys. Rev.,123 (1961) p.1373 .

(45) P. J. Campion, J. W. Knowles and G. A. Bartholomew, Bull. Am. Phys. Soc.,4 (1959) p.247 .

(46) O. Zehender and R. Fleischmann, Zeits. für Physik,188 (1965) p.93 .

(47) F. Poortmans and H. Ceulemans, Nucl. Phys.,A97 (1967) p.657 .

(48) L. Forman and F. A. White, Nucl. Sci. Eng.,28 (1967) p.139 .

(49) F. B. Simpson and R. G. Flugharty, Bull. Am. Phys. Soc., 2 (1957) p.42 .

(50) P. Cress, unpublished report, Univ. of Waterloo (1966) .

(51) J. M. Blatt and V. F. Weisskopf, Theoretical Nuclear Physics, John Wiley and Sons (1952) p.648.

(52) Ibid, p.371.

(53) Ibid, p.372

(54) A. Stolovy and J. A. Harvey, Phys. Rev., 108 (1957) p.353.

(55) A. G. W. Cameron, Can. J. Phys.,34 (1957) p.666.

(56) K. S. Toth and J. O. Rasmussen, Nucl. Phys.,16 (1960) p.474.

(57) V. N. Lutsenko, Nucl. Phys., 47 (1963) p.42.

(58) J. O. Rasmussen, Nucl. Phys., 44 (1963) p.93.

(59) J. Blomqvist and S. Wahlborn, Arkiv for Fysik, 16 (1960) p.545.

(60) M. Rho, UCRL-11080, Thesis, University of California, (1963) unpublished.